8-2018

Modeling and Characterization of High-Power Electronic Devices: System Analysis of Laser Diodes with Flash Boiling and GaN HEMT Reliability Modeling

Evan L. Schlenker
Purdue University

MODELING AND CHARACTERIZATION OF HIGH-POWER ELECTRONIC

DEVICES: SYSTEM ANALYSIS OF LASER DIODES WITH

FLASH BOILING AND GAN HEMT RELIABILITY MODELING

A Thesis

Submitted to the Faculty

of

Purdue University

by

Evan L. Schlenker

In Partial Fulfillment of the

Requirements for the Degree

of

Master of Science in Electrical and Computer Engineering

August 2018

Purdue University

West Lafayette, Indiana

THE PURDUE UNIVERSITY GRADUATE SCHOOL
STATEMENT OF THESIS APPROVAL

Dr. Peter Bermel, Chair

Department of Electrical and Computer Engineering

Dr. Timothy S. Fisher

Department of Mechanical Engineering

Dr. Daniel S. Elliott

Department of Electrical and Computer Engineering

Approved by:

Dr. Venkataramanan Balakrishnan

Head of the School Graduate Program

ACKNOWLEDGMENTS

Thank you to the Center for Integrated Thermal Management of Aerospace Vehicles (CITMAV), and its industry partners (Boeing, Honeywell, Lockheed Martin, Northrop Grumman, and Rolls-Royce), for funding the flash/laser research. Thank you to the Office of Naval Research (ONR) for funding the GaN HEMT NEPTUNE project.

Many generous individuals contributed their time to help with my research. Thanks to Kevin Koch, for assistance with working on the experimental setup and the transition into CITMAV. Thanks to Trevor Bird, for assistance in implementing the beam profiler LabVIEW program. Thanks to previous CITMAV students, including: Jeff Engerer, for the development of the original flash rig, Dan Konopa, for his steady-state laser testing, and Stephen Hodson, for demonstrating the initial flash/laser integration. Thanks to Dr. John Doty for assistance with Design of Experiments. Thanks to David Kortge for valuable insight and discussions throughout my time at Purdue.

I would like to personally thank my advisor, Dr. Peter Bermel, for his support, advice, and mentorship, beginning before I even arrived at Purdue. By his example, Dr. Bermel helped me improve as a student, researcher, and person. I would also like to thank Dr. Tim Fisher for exposing me to the mechanical/aerospace engineering industry through CITMAV and his academic and career guidance. Thank you to Dr. Dan Elliott for sitting on my committee.

Finally, thank you to my parents. I would not be where I am today without their support.

TABLE OF CONTENTS

LIST OF TABLES

LIST OF FIGURES

ABSTRACT

Schlenker, Evan L. MSECE, Purdue University, August 2018. Modeling and Characterization of High-Power Electronic Devices: System Analysis of Laser Diodes with Flash Boiling and GaN HEMT Reliability Modeling. Major Professor: Peter Bermel.

Modern electronics are increasingly more capable of high-power density operation, which presents important thermal challenges. High-power laser diode bars have proliferated in recent years, and while they can generate high optical powers, slope efficiencies are theoretically limited, resulting in high excess heat loads and consequent temperature shifts that can impair many applications. As a result, managing the ensuing heat flux and temperature changes has become increasingly important. Although traditional single-phase cooling solutions are limited by their convection coefficient to a certain temperature difference, two-phase solutions have potential for significantly higher convective coefficients. Flash boiling is a cooling method that can facilitate high levels of transient convective heat transfer, while allowing active control of coolant temperature. The transient nature of a flash cooling event is compatible with the heat load generated during operation of a high-power laser diode bar. Here, optical properties including spectral shift, spectral broadening, optical power, and beam quality are characterized over time. System inputs and outputs are correlated and evaluated via a statistical surrogate model. In certain cases, flash boiling is demonstrated to be a viable means of regulating laser diode bar temperature to achieve desirable optical output characteristics.

In parallel, GaN HEMTs have seen rapid adoption in electronics applications due to their capability to operate at high powers at quick switching rates. As power levels rise, thermal management becomes crucial to avoid long-term degradation of the device. Spatial thermal modeling can help improve long-term reliability by linking

local temperatures with various temperature dependent failure mechanisms such as hot-carrier injection.

Part I

SYSTEM CHARACTERIZATION OF HIGH-POWER LASER DIODES WITH FLASH COOLING

1. INTRODUCTION

As electronics in general grow in power density (particularly in transient applications such as power electronics, aerospace, and hybrid vehicles), an on-demand cooling solution capable of handling large, highly transient heat fluxes has potential to make a significant impact throughout the industry. Here, the focus is on understanding the transient, multi-physics interaction of a high heat flux device (in this case, a laser diode bar) with a flash cooling system. This work presents the first application of flash boiling as a cooling approach for laser diode bars and provides insight into novel physical interactions that occur in this transient system.

Laser diodes have an increasingly broad range of applications, from optical communications to high-power directed energy beams. The demand for greater power levels has resulted in the development of high-power laser diode bars, which combine tens or hundreds of quantum emitters into a single package. Peak time-averaged powers can approach 300 W within a 1-cm^2 area [1]. Because of their high efficiency, diode bars are also a common pump source for solid-state lasers (SSLs) [2]. This enables diode pumped solid-state lasers (DPSSLs) to reach capacities of 100 kW [3–5]. Now, there is great interest in modular high energy lasers capable of delivering high energies at a distance [6] whose efficacy depends strongly on beam quality [7].

However, the high current and power densities required in such devices also result in large heat fluxes that can degrade performance and damage the device, particularly under continuous wave (CW) or quasi-continuous wave (QCW) modes of operation. For example, temperature rise narrows the bandgap of the diode, leading to a redshift that disrupts the absorption of a SSL dependent on narrow spectral absorption features [8,9]. Also, spectral broadening due to inhomogeneities of the emitter surface temperature can reduce the spectral coherence of the laser [10–12]. Beam quality, which quantifies the degree of variance from an ideal Gaussian diffracted beam [7],

commonly decreases with non-uniform heating. Temperature increases can increase the threshold current and reduce the efficiency of a laser very rapidly — exponentially, in some cases [13]. As such, these negative thermal effects are extremely detrimental to overall DPSSL system performance. For an Nd:YAG (common gain medium) DPSSL, a spectral shift of only 3 nm (corresponding to a ~10 K temperature rise) can cause a large mismatch between the pump source wavelength and absorption coefficient in the DPSSL [14,15]. One might compensate for the loss of optical pump power by increasing the electrical input power to the diode; however, this results in further spectral shift, additional decrease in efficiency, and spectral broadening, ultimately leading to thermal runaway and catastrophic failure in the worst case [16]. These issues have driven a shift toward fiber lasers, which boast higher surface area-to-volume ratios, but fiber lasers may have limited power and beam quality, compared to DPSSLs.

As the demand for high-power laser diodes increases, achieving a better physics-based understanding of the interaction of cooling measures with diode operation has become of paramount importance. While there has been extensive characterization of CW lasers (dominated by thermal effects) and short-pulsed lasers (governed by quantum physics), the QCW regime at the relatively high duty cycles discussed here is underrepresented in the literature. QCW analysis requires looking at an intermediate transient window, as a pseudo-steady-state temperature is reached after a few seconds of operation. The sudden (often transient) massive heat fluxes observed in laser diode bars provide a unique cooling challenge [17]. The traditional approach to cooling, single-phase convection, is limited by the convection coefficient at the interface, h. While this method is adequate for many steady-state applications, the single-phase approach is not ideal for brief, intermittent high-power lasing events, as the cooling needs to be continually operated or cycled, and thus is unable to maintain a stable, small temperature and wavelength shift. Therefore, other approaches are needed to achieve higher performance. Two-phase cooling represents a reasonable alternative in this context [18].

Flash boiling is a specific two-phase cooling approach previously reported by Engerer and Fisher [19], among others [20–22]. The unique aspect of flash boiling is its transient thermal behavior [23, 24]. Sudden depressurization of the working fluid (methanol, in this case) decreases the saturation temperature markedly. If this process occurs quickly enough, the liquid remains at its original temperature, which is then much greater than the saturation temperature (superheat), causing a rapid phase change as soon as the liquid is depressurized [25] over a time window of approximately 100 ms. Higher superheat levels increase the rate of phase change; at higher superheats, thermal energy can be absorbed by latent heat at a faster rate. The mean fluid mixture temperature quickly drops to the saturation temperature, which can be well below ambient temperature. Nucleation begins to occur as the flash process begins [20]. As the flash process continues, the fluid cools its surroundings, which may include a transient heat source [26]. Here, the cooling effect can be tuned to the location and power dissipation of the heat source such that the latter's temperature remains relatively constant [19]. Typically, the flash results in an initial peak cooling that declines after the heat source turns off to a quasi-steady-state value [27] until the coolant supply is exhausted. A sufficient amount of coolant is necessary to avoid dryout, but too much coolant may cause the flash to not trigger. Reliable triggering of the flash event is an important part in managing a transient cooling system.

Because flash boiling operates on a similar timescale to the turn on of a QCW mode laser diode (typically hundreds of milliseconds), unique physical interactions are observed as the two transient processes interplay with each other. The system as a whole is composed of various parts operating at different timescales — for instance, heating inside the quantum well occurs on the microsecond scale, while the bulk temperature requires a few seconds to stabilize due to the presence of thermal reservoirs such as the heat spreader.

Understanding the interaction of a highly transient heat load with a dynamic cooling process provides new physical insights that could benefit the development of cooling implementations for a wide variety of high-power devices. To fully evaluate

the diode bar's optical performance and the efficacy of flash boiling for this cooling application, characteristics such as spectral shift, spectral broadening, beam quality, and optical efficiency are collected and evaluated. A rigorous statistically-designed series of experiments has been implemented to develop a surrogate model for certain optical characteristics of the system to evaluate the efficacy of flash boiling as a cooling method for laser diode bars. First, the integration of the flash boiling setup with a laser diode bar is discussed in Chapter 3. In Chapter 4, both individual and group run data are presented, with further analysis and discussion in Section 4.6. Finally, the conclusions regarding this work and recommendations for future research are presented in Chapter 5.

2. LASERS

Background information pertinent to laser operation is presented in this chapter. Basic laser theory is first discussed, followed by the workings of a semiconductor laser. Further background is then provided for high-power diode lasers and their applications in solid-state laser (SSL) systems. Next, the concept of beam quality is explored as an important optical performance characteristic. Thermal effects including spectral shift, spectral broadening, efficiency decrease, and degradation of beam quality are discussed, followed by an overview of thermal management techniques for laser diodes.

2.1 Laser and Laser Diode Theory

Lasers are devices that generate or amplify coherent infrared, visible, or ultraviolet radiation. A laser gets its name from its general operating principle - light amplification by stimulated emission of radiation. Laser beams are characterized by their high levels of directionality, spectral coherence, and intensity. These properties have led to widespread adoption in many industrial, medical, consumer, and military applications.

The key elements of a laser are: a laser or gain medium, a pumping process to excite particles in the laser medium, and optical feedback elements that support amplification or oscillation [28]. Population inversion is the driving force of laser operation. It occurs when a sufficient number of particles in the gain medium have been pumped or excited into higher quantum energy levels, such that more particles exist in the higher energy state than the lower energy state. Once population inversion occurs, certain frequencies of electromagnetic radiation can be input into the gain medium and will be amplified as they pass through, as particles from the upper quantum level transition down to the lower level. Coherent amplification means the

output signal is essentially the same as an amplified input signal (very minor phase shift, distortion, and noise are introduced). If combined with optical feedback, laser oscillation can occur where electromagnetic radiation passes through the gain medium and is amplified multiple times. Laser oscillation produces highly directional and monochromatic beams that are both bright and coherent. An example of a typical oscillator is shown in Fig. 2.1, which highlights the three key laser components.
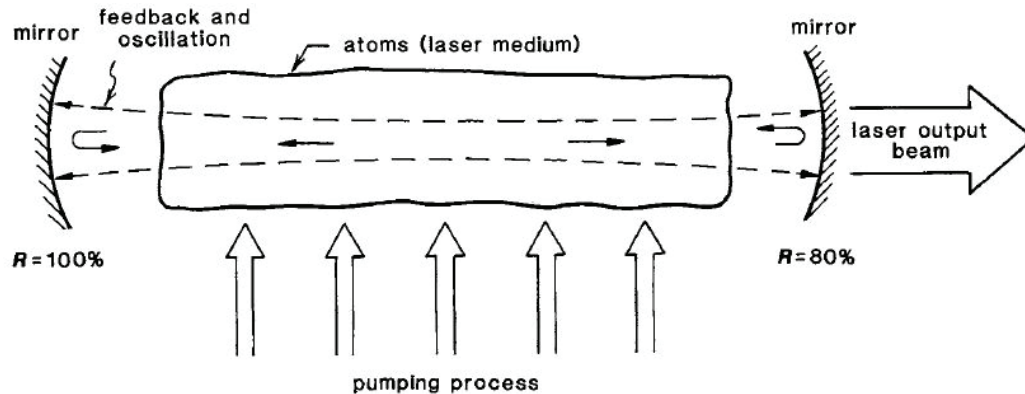
Fig. 2.1. Example of a typical laser oscillator [28].

Electrons in atoms have discrete quantum energy levels that they can occupy. In order for an atom to increase in energy level, it must absorb energy from some external source. This could be by collisions with other particles, or in the case of lasers, optical absorption. The absorbed light must coincide with transition frequencies from the ground state to the higher energy states. However, the particle on its own will soon release excess energy by spontaneous emission and drop back to a lower energy level. Excess energy is released as electromagnetic radiation at discrete spectral values, related to the amount of energy in the transition by Planck's Law

$$\omega_{21} = \frac{E_2 - E_1}{\hbar},$$

where ω_{21} is the angular frequency and E_2 and E_1 are the higher and lower energy levels, respectively [28]. The spontaneous emission process is governed by a first-

order differential equation dependent on the number of atoms in the state and the time constant for spontaneous energy decay [29].

While spontaneous emission is concerned with downward transitions and occurs at random intervals, stimulated emission covers upward and downward transitions and is dependent on incident radiation. Incident photons can excite lower energy atoms to move to a higher level, with the rate proportional to applied photon density, in the process known as stimulated absorption. Conversely, an incident photon can cause an atom in the excited state to drop to a lower state, producing a photon with the same frequency, polarization, direction of travel, and phase of the stimulating wave [29]. The emitted photon then contributes to the inputted optical signal, essentially amplifying the incident signal. Simplified examples of spontaneous emission, stimulated emission, and absorption are shown in Fig. 2.2.
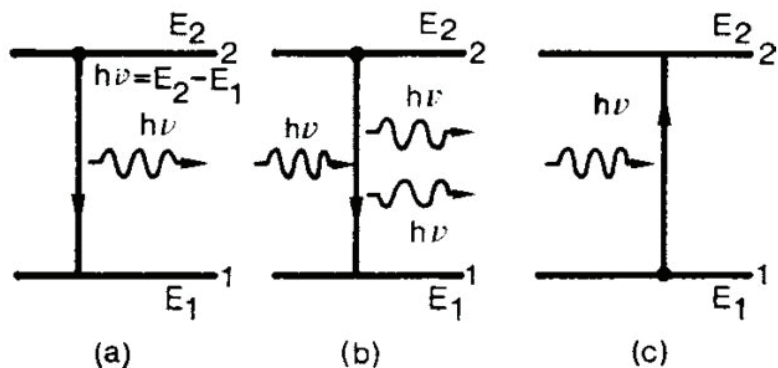
Fig. 2.2. Schematic illustration of three optical processes in a laser: (a) spontaneous emission, (b) stimulated emission, and (c) absorption [30].

If the number of atoms in the higher energy state is greater than that of the lower energy state (population inversion), then if an external signal is applied, net energy will be given up by the excited atoms and essentially added to the applied signal. This amplification is proportional to the level of population inversion (and by extension, the pumping level) as well as the strength of the input signal. The probability of both stimulated emission and absorption for a given input photon is the same; the

net flow of atoms is governed by the difference in population between high and low energy states [28]. The stimulated transition process is based on resonant responses at the atomic level, thus the net amplification is a coherent process. Spontaneous emission works in all directions, while both stimulated processes occur in the same direction as the input signal.

In the case of a laser oscillator, spontaneous emission into a cavity mode can serve as the starting point for stimulated emission. Signal amplitude increases throughout the gain medium, but there may be losses present in the cavity. If the round-trip gain exceeds the loss, the signal will exponentially grow during each round-trip, eventually reaching a coherent, steady-state. The threshold condition for the start of laser oscillation is therefore a round-trip gain greater than one. As the signal grows past laser threshold, some of the population inversion is "used up" and the gain saturates (amplifying arbitrarily large signals would require arbitrarily large pump powers), resulting in steady-state oscillations [2].

Spectral coherence is related to the laser's linewidth, which is the width of its optical spectrum. A relatively narrow linewidth indicates a high level of spectral coherence. Full width at half max (FWHM) refers to the spectral width at half the maximum amplitude and is a common measure of spectral width. Lasers in general have high spectral coherence and are often referred to as monochromatic, meaning they have narrow linewidths. Temporal coherence describes the correlation in signal amplitude and/or phase at a given reference time compared to another time. A good laser has high temporal coherence, which physically is simply manifested as a temporally stable output. Spacial coherence means a laser has a consistent amplitude and phase pattern across any transverse plane inside the laser and the output mirror. Physically, a highly spatially coherent beam will be smooth in amplitude and phase across the output. Introduction of higher order modes will reduce the spatial coherence of the laser. At higher power levels, it is common for oscillations to occur in higher order modes, resulting in a decrease in spatial and temporal coherence, and by extension, beam quality [28]. A laser operating at the ideal single-transverse-mode is

said to be "diffraction limited", which means the far-field diffraction and and focal spot size will be as close to the ideal physical limits given the laser cavity and optical parameters.

Semiconductor lasers have become arguably the most important class of lasers and are commonly featured in applications such as TV signal transmission, telephone and image transmission, computer interconnects and networks, CD players, bar-code readers, laser printers, and military projects [31]. Another common application is as a pump source for solid state lasers (SSLs). There have been a significant amount of unique diode laser types and specific designs since the first GaAs homojunction semiconductor laser was introduced [32]. Common modern semiconductor laser designs include heterojunction and quantum well varieties, which are commonly integrated with fiber lasers [33].

The core operating principle of a semiconductor is the same of that of a traditional laser: a gain medium pumped to reach population inversion is used to repeatedly amplify a signal. In a semiconductor laser, population inversion is produced in a recombination region and achieved by the injection of electron-hole pairs. Thus, the pumping process is controlled directly by electrical input, which greatly simplifies device use and allows for flexibility in the pumping process. In order to produce feedback, an optical cavity is needed. A planar mirror effect is commonly implemented by cleaving two parallel facets at each end of the active medium to form a Fabry-Perot cavity [34]. Confinement along the other axis is achieved by sandwiching the active medium between high index regions to form a waveguide. This is the design technique behind a double-heterostructure laser (a common material pairing is GaAs with AlGaAs).

If this confinement region becomes narrow enough, energy levels become quantized in the active medium [35]. Laser wavelength and other performance parameters can be tuned by altering the width of the well [36]. This flexibility in design has contributed to the widespread use of quantum well lasers in communications and laser arrays. The density of carriers increases as they are confined to a more two dimensional region.

This enables quantum well lasers to have high lasing efficiencies compared to other types of semiconductor lasers, although the total number of carriers is low due to the thinness of the active region [37]. This results in a lower overall power output, which is commonly addressed by placing many quantum wells in a single laser device.

2.2 High-Power Laser Diodes and Bars

As laser diodes have become more popular, the demand for higher power levels has increased. Increasing the width of the emitting area is one way to increase the output power of a diode laser, however this increases the prevalence of filamentation damage and modal instabilities that cause inhomogeneous power along the laser face [36]. This causes hot spots that rapidly degrade the diode laser. To increase package power density, it is common to place multiple quantum well emitters in a single device (often 20-70 emitters). Emitters can be placed in one-dimensional arrays, or as subarrays with multiple stripes containing a few emitters each. An example diode bar with common dimensions is shown in Fig. 2.3.
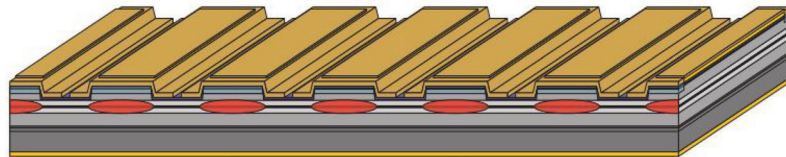
Fig. 2.3. Example of a laser bar, consisting of electrically and optically separated single emitters. The length of the bar is normally 10 mm, the resonator length between 600-1000 µm, and the spacing between emitters 50-100 µm. The fill factor (the ratio between the optically active area to the whole area of the bar) is between 30 and 50% [36].

There are many manufacturing applications for high power diode lasers, including plastic welding, brazing, and cutting [38]. Fig. 2.4 shows some of the various applications for high-power diode lasers. The various applications can have a wide range of power and beam parameter product (BPP) requirements. The BPP is the product

of the divergence angle and radius at the narrowest point (waist) of the beam, and is a measure of how well the laser can be focused (beam quality).
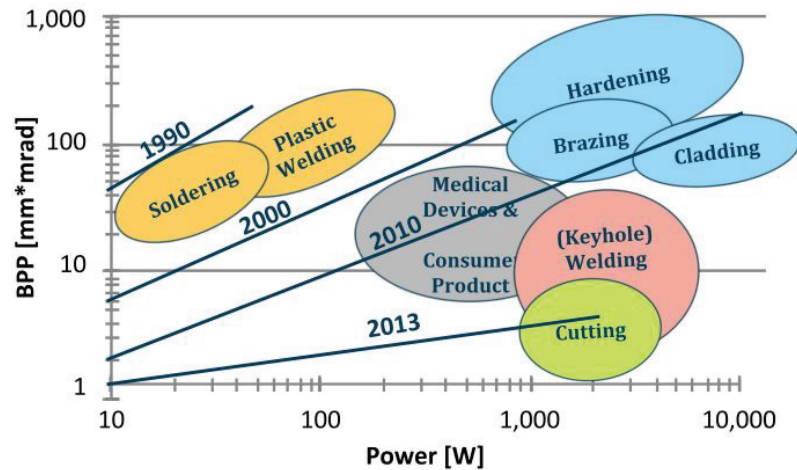
Fig. 2.4. Applications of diode lasers based on power and Beam Parameter Product (BPP), which is a measure of the laser beam quality [38].

2.2.1 Solid-state laser systems

There have been numerous laser directed energy weapon (DEW) projects since the 1970's amongst different military and research groups. In addition to missile defense, SSLs are used in target illumination and remote sensing. The first Sparta/Zeus system implemented a 500 W Nd:YAG SSL for destruction of unexploded ordnance at up to 250 m, while newer systems can be over 10 kWs [39]. Projects exceeding 100 kW are in the works [3,5,6]. SSLs use a doped crystalline or glass material. An external power source pumps ions to an excited state that are later emitted as laser radiation. A SSL does not need to operate for long periods of time - in close range applications, the calculated time to "kill" is on the order of seconds [39].

One of the most common applications of high-power diode lasers is as a pump source in a diode-pumped solid-state laser (DPSSL) system [4]. Advantages of diode

lasers compared to other pump sources include small size, high efficiency, low voltage, narrow spectral width, and long operating lifetimes. In 2015, diode bars designed for pump applications reached power levels of 300 W [1]. As of 2018, 1 cm diode bars at near-infrared wavelengths capable of 500 W peak power exist that have been demonstrated to have a 63% operating efficiency, although at a duty cycle of 0.75% [40]. Many pumping applications, such as DPSSL, hybrid lasers, and fiber lasers, utilize pumping in the Quasi Continuous Wavemode (QCW) regime, where the output consists of long pulses that appear nearly continuous to the eye, but in fact are pulsed due to modulating the input signal. This reduces heating and allows for operation at higher peak powers. High fill factors (>75%) and operation at a duty cycle under 20% is common for DPSSLs [40]. Arrays with large fill factors are preferred for short-pulse, high peak power operation, while lower fill factors are ideal for long-pulse, high average power operation [41]. In a SSL pumping application, spatial coherence is not as important due to the relative flexibility and accessibility of physical connections with diode lasers, however, spectral coherence is extremely important in pumping efficiency [42].

GaAs/InGaAs lasers are commonly used as QCW pump sources for Yb:YAG [17] and Nd:YAG SSLs because the typical emission central wavelengths overlap well with the absorption profile of the SSL gain medium. Pumped light that does not fall within the absorption profile is absorbed as waste heat and reduces the efficiency of the system. It can also cause thermal aberrations that reduce the output laser beam quality. Thus, a critical design aspect of a DPSSL system is ensuring the pump wavelength remains at the absorption peak and that the emission spectra does not broaden outside the absorption peak. Reducing the spectral width of a pump diode allows for improvement of compactness, efficiency, power, and beam quality in a SSL system [15]. Fig. 2.5 shows how the absorption characteristics of an Nd:YAG laser medium interact with the emission spectra of a 808 nm diode bar.
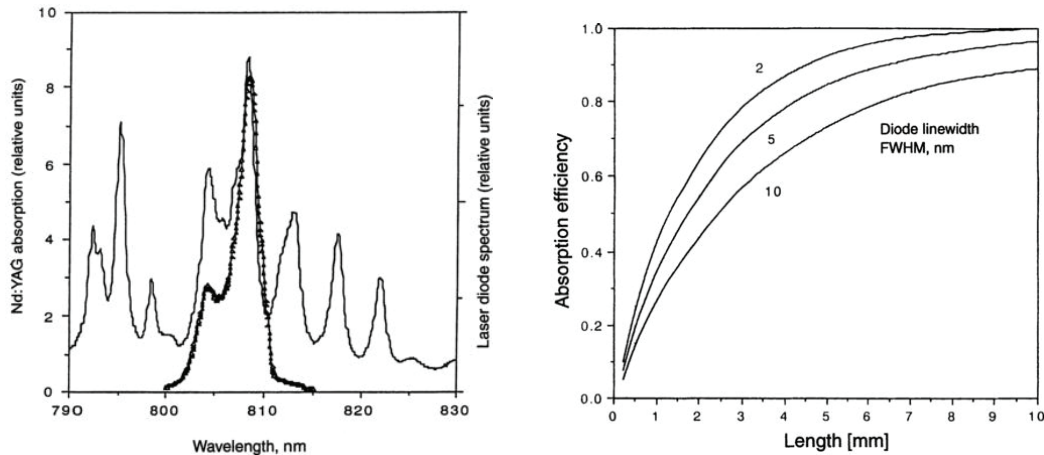
Fig. 2.5. Relevant Nd:YAG absorption characteristics for a DPSSL application [2]. (a) shows the spectral overlap of the Nd:YAG absorption profile and the sample emission spectrum of a GaAlAs 808 nm laser array, while (b) shows the absorption efficiency compared to pump length for a 808 nm pump wavelength, at various spectral widths.

2.3   Beam Quality

There are different ways to define beam quality, but all definitions generally encompass how well a laser beam can be focused. As mentioned at the end of Section 2.2, the BPP is one measure of beam quality which is quantified by the product of the beam radius at the beam waist (minimum radius of the beam along the beam path) with the far-field divergence angle. The best values for BPP will be small but depend on the operating wavelength. A slightly more common definition is M^2, which is the BPP normalized by an ideal diffraction-limited Gaussian beam of the same wavelength. An ideal beam has an M^2 of 1, so values closer to 1 are most desirable for applications requiring highly focused beams. A high power semiconductor laser can easily have a very large M^2 of more than 100, or 1000 in some cases, due to broad area radiation and large divergence angle [43]. There are markets for high-power diode lasers both in low and high beam quality applications. For the high beam quality applications, advanced beam shaping is necessary to handle the

wide emission angle and high power levels of a laser diode [44]. High-power diode bars have both a fast and a slow axis, typically having better beam quality along the fast axis [30]. Optics such as collimating and focusing lenses are commonly used to handle the highly divergent light associated with a high-power laser diode. Since the BPP is optically invariant, adding additional optical components cannot improve beam quality and in many cases, can actually degrade it [45].

The establishment of consistent experimental beam quality definitions has been a challenge in laser characterization for a long time. Part of the confusion stems from the lack of a consistent beam width measurement technique. In order to determine M^2, beam widths are fit to a Gaussian propagation equation modified with an M^2 propagation factor. For real-world beams, different measurement methods and definitions will produce different beam widths. Some possible definitions include: width (or half-width) at first nulls, variance σ_x of the intensity profile in one or the other transverse direction, at $1/e$ or $1/e^2$ intensity points, the D86 diameter, transverse knife edge widths, or some kind of best fit Gaussian. Formal M^2 measurements require multiple second moment width measurements, however accurate second width measurements can be hard to achieve. CCD issues such as background noise, baseline drift, camera nonlinearity, and digitization measurement errors affect consistency in sampling. The second moment method also heavily weights the tails - discontinuous beams may even have a seemingly infinite M^2, although this is unrealistic [7]. Regardless of these difficulties, the ISO11146 standard advocates for a second moment based, 10 measurement procedure for determining M^2 [46].

Despite this standard, many scientists use their own methods or black box equipment for M^2 measurements, so it is sometimes difficult to compare these measurements across works, unless the author is explicitly using the ISO standard. As mentioned, the second moment method weights small amounts of noise away from the beam more heavily than the beam that is actually being analyzed. Averaging columns of the CCD to find the appropriate artificial "zero" defines a "noise equivalent aperture" and reduces the maximum contrast available for analysis [47]. Without knowing

the beam width in advance, it is easy to ignore relevant parts or modes of the beam. The noise equivalent aperture is a function of peak power, so neutral density filters are recommended to attenuate the beam to maximize the contrast and keep a relatively constant noise equivalent aperture. Some argue that M^2 is typically only accurate to slightly better than 1 significant figure [47]. In summary, M^2 is the most widely used method of measuring and describing beam focusability, but may not always be the best characterization choice, depending on the application.

2.4 Thermal Effects

It has been established that high-power laser diodes are desirable for many applications due to their high power levels and small device sizes. These high heat fluxes inherently present difficult thermal management challenges. Because typical quantum well areas are on the order of just hundreds of square microns, heat flux densities for diode laser emitters can reach values of several kW/cm^2, which is comparable to the surface of the sun [48]. Heat fluxes for different events are shown in Fig. 2.6 for reference. Note the relatively lower temperature associated with laser diodes, which complicates heat removal even further. If handled improperly, these high heat loads can cause damage to the device and reliability issues, as well as reducing efficiency, inducing wavelength shift and spectral broadening, and degrading beam quality.

Thermal issues are the main factor limiting the increase of the fill factor in diode bars. Increasing current levels in individual emitters causes the temperature in the active region to grow, reducing carrier confinement and increasing the rate of nonradiative recombination processes. This decrease in efficiency eventually results in output power saturation known as thermal rollover. Using higher fill factors is generally better for high peak power operation, as it minimizes the temperature rise in the active region [49]. However, too high of a fill factor will cause heat generated from each emitter to spread to adjacent emitters, resulting in a large temperature rise in the emitters.
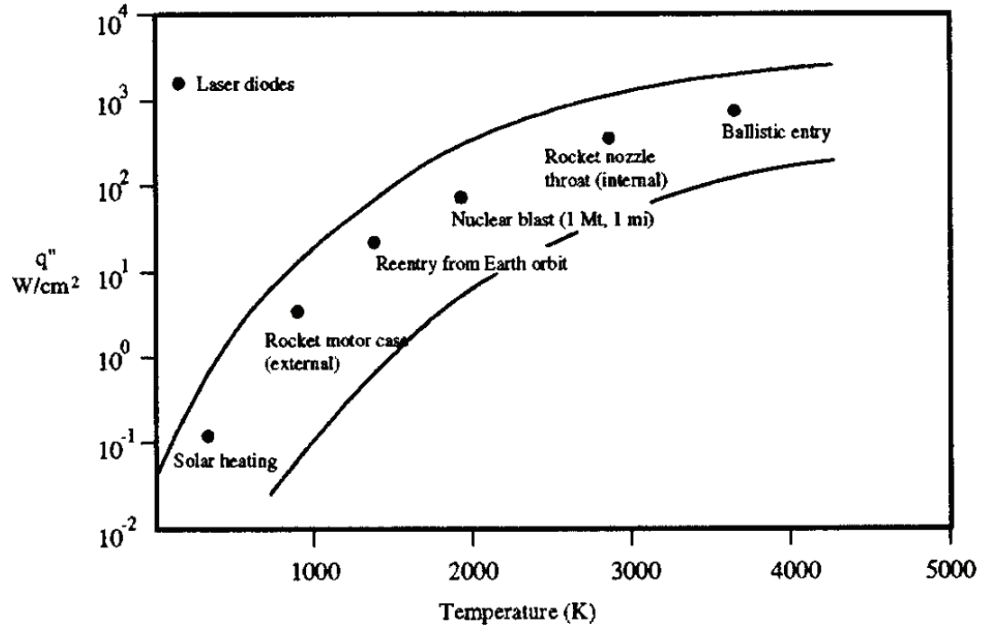
Fig. 2.6. Heat fluxes for various events as a function of temperature [48].

Current flowing through a diode laser can cause heating in three distinct ways [50]. Heat is generated at the junction due to inefficiencies in the light generation process, whose efficiency is dependent on the quantum efficiency, the current density, and the voltage drop across the junction. The bulk resistivity and contact resistance are the other two sources of heat generation. As current levels increase, the temperature rise at the contacts can potentially exceed the temperature rise in the junction in a homojunction laser [50]. Thus, while the junction may be relatively cool, the diode may still be susceptible to damage due to thermal effects from the contacts. In a double-heterostructure device, above the lasing threshold, the temperature distribution narrows around the active region and the heat source is concentrated around the active region [51]. In a quantum well laser, self-heating is primarily due to non-radiative recombination in the quantum wells, reabsorption of emitted photons, and ohmic losses (generally in the bulk material) [52]. At higher current levels, heating mainly occurs due to series resistance and from absorption of the laser light, especially

in the vicinity of the cavity mirrors [36]. The temperature is usually not constant along the active region.

Heating in the transient regime further complicates analysis. It is also not straightforward to measure the temperature of the active region due to its small size and rapid transients, although recent techniques such as thermoreflectance measurements [53] and superposition of current pulses [52] can help quantify temperature in the active region. Heating in the active region occurs on the order of microseconds [10]. For pulse times greater than 1 μsec, thermal diffusion maintains the junction at a uniform temperature [54]. The two primary types of "cm bars" are actively (convectively) and passively (conductively) cooled. Each type has very different thermal properties. A steady-state thermal situation is established after about ~30 ms in actively cooled laser bars and several seconds for passively cooled bars (with pulse widths low enough to ensure thermal relaxation), although this can vary substantially based on device geometry, pulse conditions, and cooling parameters [55].

2.4.1 Efficiency

Depending on the thermal resistance of the device and the generated waste heat, the temperature of the active region may rise, leading to a reduction in carrier confinement and increase in the amount of nonradiative recombination [36]. Non-radiative recombination directly contributes as heat, while a reduction in carrier confinement reduces the number of electrons available for lasing. Both processes increase the threshold current and decrease the slope efficiency, which is the ratio of optical power to the current above the threshold current [43].

The laser threshold current I_{th} is the current required to achieve enough gain to match the resonator losses and begin lasing. An increase in threshold current can significantly increase the dissipated power and therefore generate heat. The threshold current increases with temperature in the active region due to a reduction in gain available at any frequency at a fixed current. Charge carriers occupy low and high

energy states based on Fermi-Dirac statistics [56], with a probability of occupancy given by the Fermi function,

$$F(E) = \frac{1}{1 + e^{(E-E_f)/kT}},$$

where E_f is the fermi energy where the probability of occupation by an electron is exactly one half. At a given temperature, the carrier distribution extends into higher energy states, as lower energy states fill first. At large temperatures, carriers are more likely to populate higher energy levels, which reduces available gain at the lasing wavelength and causes this increase in threshold current [57]. This is also the process responsible for the increase in carrier leakage at higher temperatures. The following empirical relation describes the increase in threshold current due to temperature rise:

$$I_{th}(T + \Delta T) = I_{th}(T)e^{\Delta T/T_0},$$

where $I_{th}(T)$ is the threshold current at the temperature T, $I_{th}(T + \Delta T)$ is the threshold current at a higher temperature $T + \Delta T$, and T_0 is the characteristic temperature parameter, which is dependent on the heterostructure design of the quantum wells [42]. The shift in threshold current in response to changes in temperature can actually be used to estimate the temperature in the active region [58].

Through these effects, temperature rise results in an increase in threshold current and a decrease in slope efficiency, as shown in Fig. 2.7. These effects can lead to further heat generation at higher current levels. In addition, the series resistance contribution to heat generation increases at higher current levels, which leads to further temperature rise and reduction in efficiency. This process ultimately limits the maximum power of the laser and is known as thermal rollover. Once output power saturates, further increase in pumping current can actually decrease due to more carrier spillage from the reduction in carrier confinement [42]. Externally reflected laser emission can also cause heating in the diode. In summary, self-heating has strong negative effects on laser characteristics like threshold current, output power, and efficiency, mainly due to non-radiative recombination, reabsorption of emitted photons, and ohmic losses. [59].
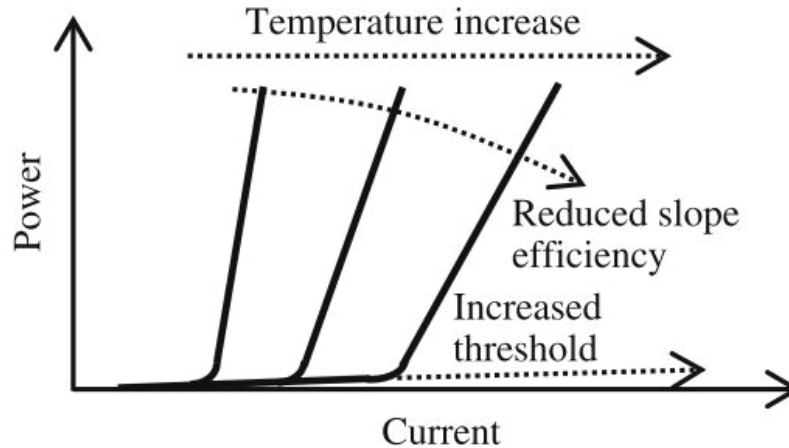
Fig. 2.7. Increasing temperature causes a rise in threshold current and a reduction of the slope efficiency in the laser diode [37].

2.4.2 Spectral shift

As temperature changes in a laser diode, the spectral output shifts. An increase in temperature leads to longer central wavelengths, or red-shift, while a decrease in temperature leads to blue-shift. In a DPSLL application as described in Section 2.2, a shift beyond only 2-3 nm has a massive impact on the absorption efficiency of the system. Temperature change in the active region is responsible for the shift, but because it is often difficult to measure, this temperature is often given in reference to some kind of steady-state cooling method. In a transient scenario, observed changes in the coolant temperature may not have immediate obvious impact on the central (or peak) wavelength due to thermal masses and capacitances in the diode assembly. It can also take several hundred milliseconds to achieve a pseudo-steady-state temperature in the active region of a laser array [60].

A measurement for the *average* value for the active region temperature can be obtained by observing the spectral shift. For GaAs/InGaAs diodes, a spectral shift of $d\lambda/dt = 0.254$ nm/K has been demonstrated [8, 60], although a commonly reported

value is $d\lambda/dt = 0.27$ nm/K [14]. The reason for this shift stems primarily from the well-known Varshni equation:

$$E_g(T) = E_0 - \frac{\alpha T^2}{T + \beta},$$

where $E_g(T)$ is the bandgap at temperature T, E_0 is the bandgap at 0 K, and α and β are material constants [9]. A decrease in bandgap energy due to higher temperatures thus leads to an increase in wavelength, based on another well known physics equation, the Planck-Einstein relation. This equation was given in Section 2.1, but can be re-written in a more applicable form here:

$$E = \frac{hc}{\lambda},$$

where E is the bandgap energy, h is Planck's constant, and λ is the associated wavelength. Heating effects also can change the mechanical length of the resonator and the refractive index, which have minor effects on spectral shifts compared to the bandgap change, but can create additional emission modes over continued heating [8]. Fig. 2.8 shows an example of spectral shift for a 808 nm laser, where red-shift occurs as temperature rises.

2.4.3   Spectral broadening

In addition to shifting of the peak wavelength, temperature rise can also cause spectral broadening. The spectral width (FWHM used in this work) increases with temperature as a result of thermal inhomogeneities along the active region. Spectral broadening of laser arrays results from the contribution of non-uniform wavelengths from individual emitters to the average output spectrum. For example, emitters toward the edges of the array might experience a smaller red-shift than those in the center, evidence of a lateral temperature gradient along the bar (although this can vary with cooling techniques) [8]. Both purely thermal bandgap shift and thermal stress effects contribute to spectral broadening. Tensile stress and compressive stress due to thermally induced mechanical stress cause red-shift and blue-shift, respectively
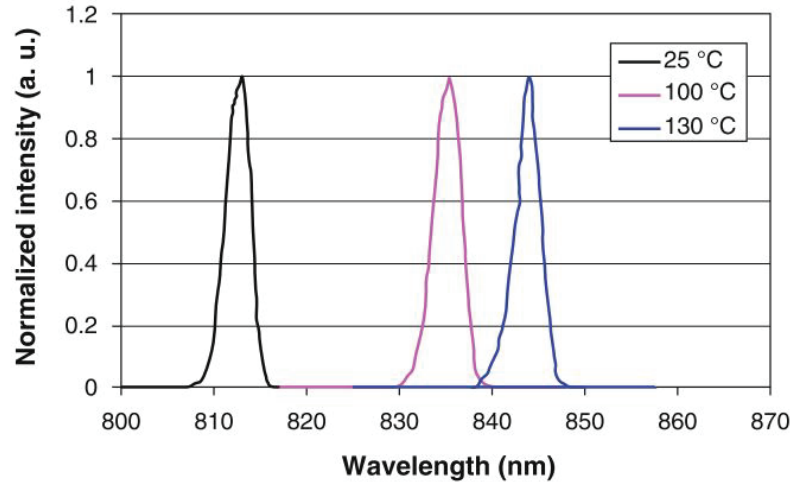
Fig. 2.8. Output spectra for a single 808 nm semiconductor laser at three distinct operating temperatures [15].

[15]. Uneven thermal stress can therefore cause minor wavelength variations across emitters in a diode bar and by extension, spectral broadening.

Another cause of spectral broadening is solder voids due to manufacturing defects. A solder void is essentially a pocket of air in the solder layer, which has a much lower thermal conductivity than the surrounding solder. This leads to thermal stresses and non-uniformity in the temperature distribution as heat accumulates around the voids. Typically, the failure of a packaged laser diode system is due to interrelated electro-thermal-mechanical-material reasons. Temperature cycling of a packaged laser bar using a soft solder causes creep and stress relaxation that ultimately cause mechanical deformations and thus variations in optical emissions across the bar [61]. These solder voids can also increase the thermal resistance of a device by over 30%, in some cases; thus, minimizing the thermal resistance of the heat sink and eliminating solder voids during manufacturing is an effective way to decrease the thermal resistance of a device [14]. Advanced laser packaging uses hard solders to minimize the thermal deformation and stress associated with solder voids. Fig. 2.9 shows an example of

the non-uniformity in temperature across the quantum well emitters of a 60 W diode bar.
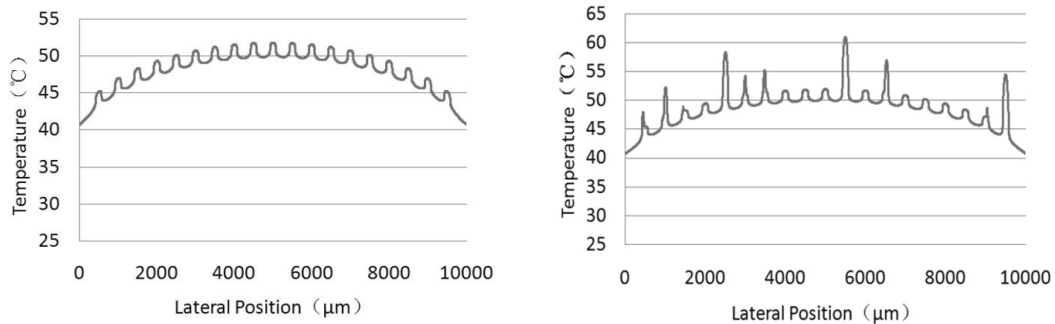
Fig. 2.9. Non-uniform temperature distribution for a 60-W CW, 808 nm laser bar is shown in (a). This thermal inhomogeneity will result in spectral broadening. In (b), a similar device with solder voids introduced demonstrates the significant impact they can have on a lateral temperature profile [14].

Most 808 nm bars have a FWHM specification of <3 nm. A broadened spectrum can (but does not necessarily) have multiple peaks and shoulders or tails at either side of the spectrum. Shoulders or tails below the FWHM value make the FWHM measurement significantly less meaningful, and the FW90%E measurement is often used instead (90% of total energy width) [15]. A high quality spectral output will have an approximately Gaussian shape, with no peaks or tails.

2.4.4 Beam quality

Finally, beam quality also degrades with temperature, due to a few intertwined mechanisms. First, thermal stress can affect the optical quality of the device by mechanical expansion and changes in refractive indices. Deformation of optical elements due to thermal stress causes wavefront aberrations, which influence the beam quality of a laser [62]. Due to temperature and optical non-uniformities (non-ideal spacial coherence) across the active region, the level of carrier population and thus the gain

and refractive index can vary [42]. At a local optical intensity maximum, the carrier density is at a local minimum. This causes decreased gain and increased refractive index. The increase in refractive index creates a local waveguide and essentially acts like a focusing lens, narrowing the mode. This causes a narrower, more intense peak in a process called self-focusing. These peaks (local maxima) then cause a local decrease in gain, or spatial hole-burning. Together, self-focusing and spatial hole-burning can result in tightly confined, individual peaks of emitted light that significantly hurt beam quality in a process called filamentation. The variance in intensity coincides with wavefront modulation in the form of multimode operation. These higher order modes cause optical aberrations in the beam, reducing beam quality [42]. An ideal laser outputs a single-transverse-mode (often Gaussian). This diffraction limited case represents the highest possible beam quality. Phase shifts in the output beam increase with greater degrees of multimodal operation, which has a significant effect on far-field beam size and therefore beam quality [28].

2.5   Thermal Management and Relevant Work

Cooling solutions are necessary in order to utilize high-power laser diodes effectively by minimizing the occurrences of the negative thermal-induced effects discussed above. Proper cooling is also necessary to ensure device reliability, which is particularly critical in military and aerospace applications. Reliability and lifetime of high-power diode laser bars are effected by operating temperature, mounting stress, and solder electromigration [63]. In general, for a high-power laser diode, the junction temperature must stay below 50 ℃ [2], and below 55 ℃ to ensure lifetimes of over 10,000 h [63].

For relatively low-power devices, passive cooling through a copper heatsink to the ambient environment may be possible. Active cooling is necessary for higher powers. Single phase forced convection is popular in aerospace power cooling for heat fluxes under 600 W/cm^2, if isothermality and very high coolant flow rates are not of

concern [64]. This approach can work in certain cases, but is limited by the convection coefficient, h, and temporal inflexibility.

Peltier coolers (thermoelectrics) work well for communications and are easy to package, but can require significant power to sufficiently cool high-power devices. Spray cooling can handle higher heat fluxes, but requires more maintenance. Microchannel coolers can work in high-power pumping applications, but in certain cases structural fabrication can be difficult for a given power/heat load application. Large pressure levels and gradients are of concern in microchannel cooling solutions [48]. Heat pumps can generally work at much higher temperature and power levels and operate reliably at high efficiency, but the rate of heat removal may not be fast enough [65].

Two-phase cooling takes advantage of latent heat for greater heat extraction potential. There are a number of techniques that have been tested for electronics cooling applications. Mudawar et al. have extensively studied two-phase cooling in microchannel heat sinks [18, 66, 67]. Erosion in the microchannels and buildup of nanoparticles can cause failure in such devices over long term operation. The group has also analyzed two-phase spray cooling and compared it to jet cooling for electronics applications [68, 69]. Spray cooling is a promising cooling solution for electronics and is already used in some high-flux applications. However, some drawbacks include clogging or wear in the nozzles and complex system design.

There is no literature regarding flash boiling for a laser diode cooling application, and only tangentially related work for using flash boiling to cool electronic devices in general (usually simply a heat load). Flash boiling has the advantage of rapid triggering of the cooling event, with very high transient convective coefficients, making it a potentially great match with a transient heat load associated with a laser diode bar. It also gives rise to more complex interactions, which will be studied in the coming chapters.

3. METHODS

3.1 Flash Hardware Setup

As previously mentioned, the original flash setup was created by Jeff Engerer and described in detail in [19]. This version of the setup was built on a mobile cart that attached to the main CITMAV board via a stainless steel Swagelok fitting that coupled the setup to a helium tank. For this experiment, the rig was moved to an optical table and a new helium line connects to the tank. Setup on the optical bench is necessary for consistency in optical characterization. The flash rig is primarily constructed from 316 stainless steel tubing and Swagelok compression fittings. These provide strong corrosion resistance and support low vacuum levels throughout the system. A stainless steel sealed vessel functions as the methanol reservoir and stores approximately 1.5 L of methanol. The tank is kept slightly above ambient pressure with helium to avoid air exposure. Methanol is chosen as the working fluid due to its stability at standard temperature and pressure (STP), and its relatively high latent heat of vaporization. A bi-directional valve connects a 5 mL Hamilton syringe to the methanol reservoir and polycarbonate flash chamber. This setup facilitates dosing a precise amount of methanol directly into the flash chamber. A solenoid valve controls a helium inlet into the flash chamber, which is used for pressurizing the chamber before a flash event, as well as purging the flash chamber after a flash event. An additional solenoid valve is connected to a vacuum tank, which is used in the purging process. The system is always kept slightly above atmospheric pressure with helium to avoid dissolved oxygen in the methanol that may affect the boiling process. The primary connection between the flash chamber and the 11.4 liter vacuum tank is a pneumatic valve. This connection allows for the sudden exposure of the flash chamber to vacuum necessary for a flash event to occur. A vacuum pump is connected to the

vacuum chamber. Numerous valves allow for control of the pump outlet flow. A valve was added to allow disconnection of the pump entirely if a constant volume is desired throughout a flash event. Further 80/20 supports were added for stability and integration with the laser components. The full system integrated with the laser setup is shown in Fig. 3.1.
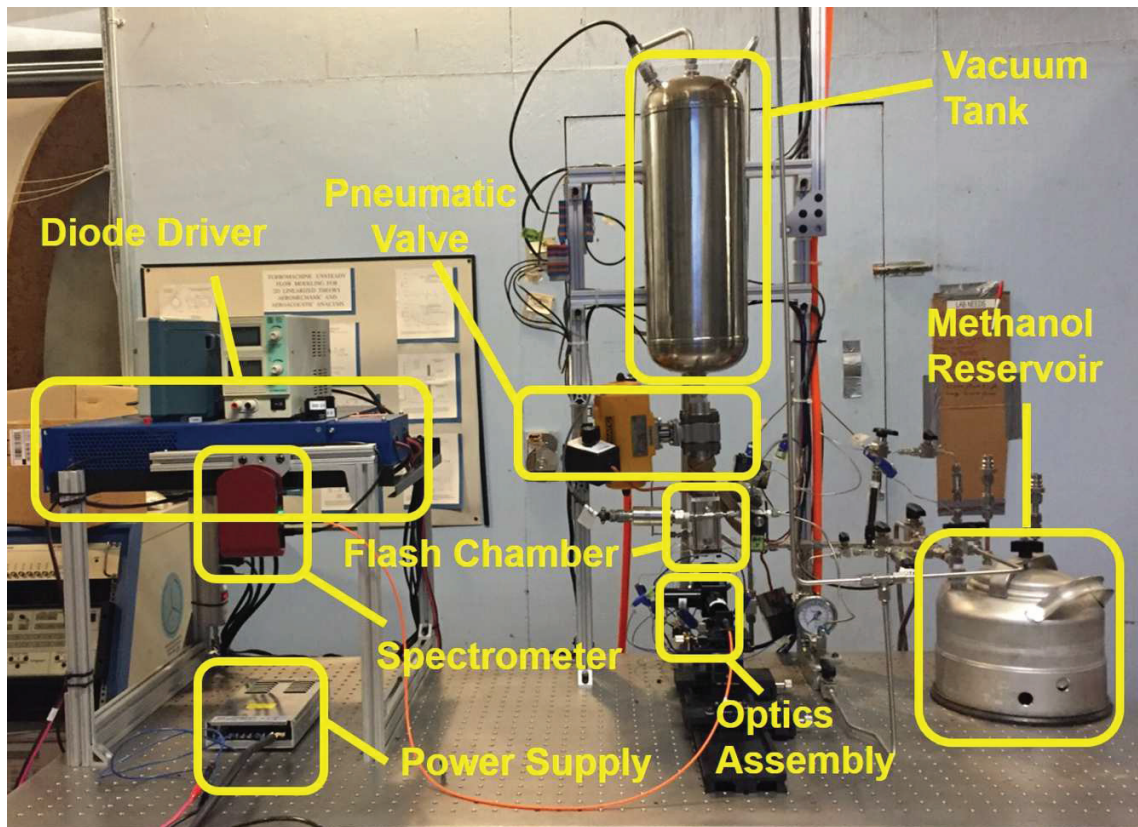
Fig. 3.1. Flash boiling laser diode test setup on top of an optical table. Helium and compressed air run directly to the setup. An oscilloscope sits above the diode driver to verify proper pulse generation via current feedback. Adapted from Engerer and Fisher [19].

3.2   Laser Diode and Power Interface

The laser diode bar used in this study is a Golden Bullet submodule produced by Cutting Edge Optronics (CEO, a division of Northrop Grumman). The ASM232P200 is a 200-W Quasi Continuous Wave (QCW) diode bar designed to be operated at a maximum pulsed duty cycle of 15%. The package design is optimized with expansion matched materials and a hard solder to reduce failures under rapid temperature change associated with diode bars. The bar's footprint is approximately 10 x 6.35 mm, while the active emitter region is 9.6 x .01 mm (0.15% of the total area). The central lasing wavelength of 808 nm for this diode bar is specified to within a tolerance of $\pm$ 3 nm. The Golden Bullet, its specifications, and its efficiency curve from the packaged datasheet are shown in Fig. 3.2, Fig. 3.3, and Fig. 3.4, respectively.
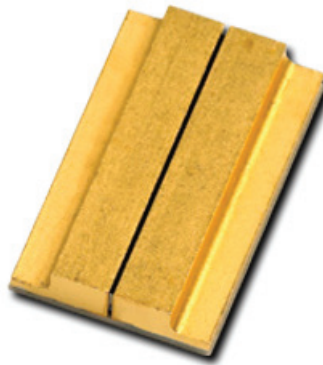
Fig. 3.2. Golden Bullet diode bar from Northrop Grumman Cutting Edge Optronics.

A copper heat spreader (brazed with a carbon foam to increase nucleation sites) is placed at the bottom of the flash chamber [19]. During operation, this vertical orientation forces liquid methanol to rest on the foam atop the spreader, so vapor will rise out of the flash chamber into the vacuum chamber. Because of the vertical flash chamber orientation, the diode must be mounted to lase straight down. A silicone
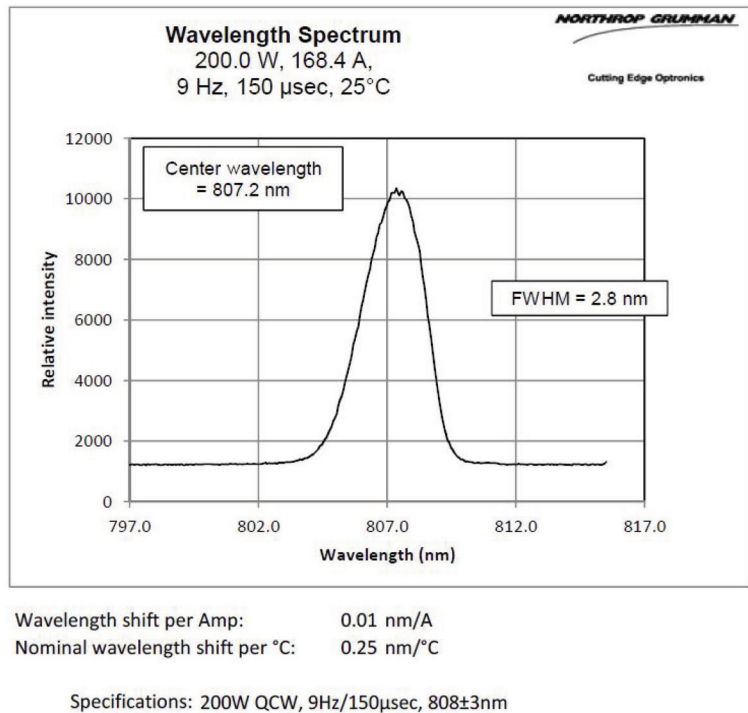
Fig. 3.3. 200-W QCW CEO Golden Bullet specifications for the actual experimental devices at 25℃.
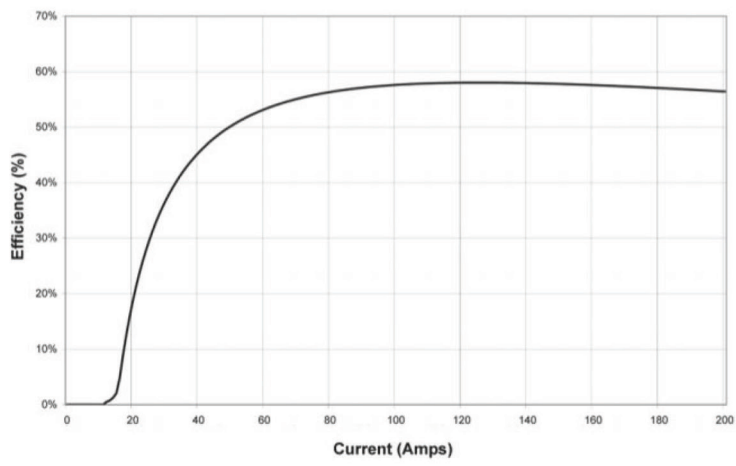
Fig. 3.4. 200-W QCW CEO Golden Bullet efficiency vs current plot at 25℃.

grease thermally conductive paste, Omegatherm 201, is used to attach the diode bar to the copper heat spreader, while providing good thermal conductance. Electrical contact is achieved with 1-mm thick copper pieces, held in place by the polycarbonate fixture screwed into the bottom of the flash chamber, shown in Fig. 3.5. The mount also provides enough pressure to secure a thermocouple to the surface of the diode with low thermal contact resistance. The copper electrical contacts are soldered to the wire outputs of the Cutting Edge Optronics eDrive laser diode driver. The driver provides precise control over the pulse characteristics and is powered by a 28-V, 350-W DC supply.
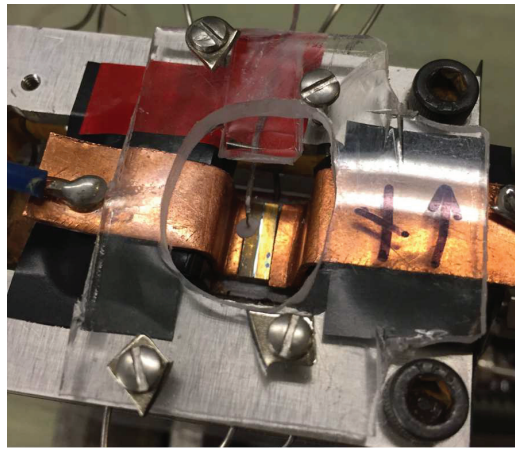
Fig. 3.5. Bottom of flash chamber, showing laser diode with thermocouple attached to copper heat spreader and copper contacts held in place by polycarbonate mount. The laser emits light directly downwards towards the plane of the optical bench.

3.3 Optics Setup

The inverted orientation of the diode bar and adjoining flash chamber requires careful design of the laser characterization setup. First, a 25-mm focal length lens is used to collimate the rapidly diverging beam emitted from the diode bar. A right-angle mirror then brings the beam into the plane of the optical table. A cubic beam-

splitter subsequently divides the beam 50/50. Each exit port of the beam-splitter includes threaded neutral density (ND) filters that attenuate the beam achromatically to avoid saturating or damaging the imaging devices. These Newport ND filters are made with Schott-Borofloat glass, which allows them to handle high instantaneous peak power levels without reaching the laser damage threshold. Fig. 3.6 shows the optics setup that is used during a typical experimental run. Not shown is a series of beam blocks placed around the optical table for safety purposes.
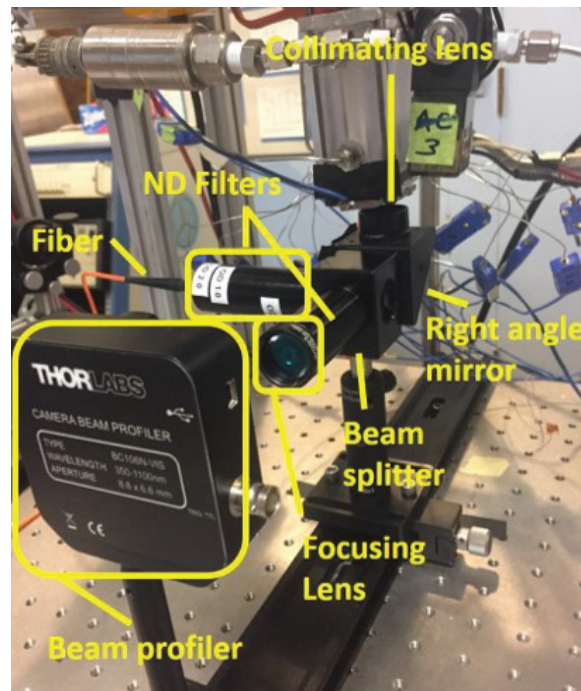
Fig. 3.6. Optics system setup. This setup is used to obtain beam spectra and beam profile images. The laser diode lases downward into the collimating lens.

3.3.1 Spectrometer

At one of the beam-splitter exit ports, a Thorlabs CCS175 CCD spectrometer is connected through free space-coupled optical fiber. Significant coupling losses are

tolerable here, as the power levels necessary for the spectrometer are orders of magnitude below the total laser diode bar emission. In prior steady-state experiments, a monochromator was adequate for analysis, although this approach required over ten repeated measurements and had a 1-nm resolution [57]. It may also have introduced uncontrolled errors if the process varied from run to run. This spectrometer captures relative wavelength amplitudes across its entire operating range of 500-1000 nm simultaneously using a Czerny-Turner system architecture, which eliminates the need for repeated spectral measurements and introduces the capability for temporal spectral sampling. A scan rate of 200 Hz is supported over USB, with 3648 CCD pixels for a pixel resolution of 6 px/nm. The worst case specification accuracy is <0.3 nm, although Thorlabs expressed the accuracy can be trusted roughly to ~0.1 nm. The CCS175 is shown in Fig. 3.7(a).

3.3.2 Beam profiler

Following the other beam-splitter exit port is a lens (f=20 mm) that focuses the beam onto a Thorlabs BC106N-VIS CCD Camera Beam Profiler. A CCD profiler was chosen to provide a more precise beam profile and a true 2D analysis of the image profile, compared to a scanning slit profiler. It features rotating ND filters, which combined with exposure and gain adjustments, eliminate the need to adjust the external ND filters attached to the beam splitter during system operation. This approach greatly reduces the risk of uncontrolled changes to the beam path during a series of experimental runs. The beam profiler is shown in Fig. 3.7(b).

The beam quality factor M^2 is calculated using beam width measurements at two distances, according to the following equation:

$$M^2 = \frac{4\pi\sigma_0\sigma_z}{z\lambda},$$

where σ_0 is the beam waist, σ_z is the beam width at distance z from the waist, and λ is the operating wavelength [70].

While the term M^2 is used to denote beam quality, it is important to note this is not a rigorous, ISO standard measurement. Most off-the-shelf beam quality measurement devices take at least 20 seconds to operate for a rapidly pulsed or CW system. Few options currently exist for turnkey QCW beam profile analysis in the transient (~5 second) regime of interest here. Therefore, a custom transient beam profiling system based on first principles with available off-the-shelf components was developed as follows.

Traditional or ISO standard width measurements for a beam quality application would employ calculation of the image variance (D4σ) at multiple distances [46]; however, the rapid divergence of the beam from a diode bar means that the profile tails will be weighted excessively. In addition, the standard prescribes that the beam be warmed up for an hour before measurement to ensure consistency between measurements, which is obviously not feasible in a case with a high-power density device with a transient cooling solution [47]. In this case, the important aspect of the analysis is not to have an absolute, industry standard beam quality, but rather a consistent measurement for the setup that can be observed and characterized over a course of experiments. Thus, to avoid excessive experimental repetition and introduction of variance, measurements are taken at the beam waist and in the far field, as described in [70]. Beam widths are found by summing the transverse image planes to generate profiles. After offsetting the profiles by subtracting the minimum profile amplitude value, a single term Gaussian is fit to the data to calculate a beam width. The goodness of fit (R^2) values for a 1-term Gaussian fit are above 0.8 for the waist, and 0.9 for the far-field. Therefore, this Gaussian approximation is sufficient and likely accurate in this application. Another possibility is a 2-term Gaussian fit, where R^2 values are usually above 0.95. The 2-term Gaussian fits the data better, of course; however, using the 2-term fit to calculate beam quality is less consistent, as the amplitude of each term can vary substantially with input conditions and between runs. Thus, the 1-term fit is employed instead. Beam quality is only calculated in the vertical (y)

direction, as the horizontal (x) profile diverges so rapidly that it quickly exceeds the profiler aperture size.

3.3.3 Power meter

For power measurements, the rest of the optical setup is removed, and the detector is placed directly under the diode to minimize losses. The meter used is a Thorlabs PM100D, controlled from a computer. Two types of detectors are used for verification purposes. A Thorlabs ES220C pyroelectric energy sensor, which converts light to voltage pulses, is optimal for high energy pulses at very low repetition rates. It has a maximum frequency of 30 Hz, a maximum input power of 3 W, and a 20-mm aperture, but a rapid response time and high precision. The other detector is a Thorlabs S314C thermal power meter, which can handle average powers of up to 40 W and has a 25-mm detection window, but has a slightly slower response time. The power meter is shown in Fig. 3.7(c).

(a) Thorlabs CCS175   (b) Thorlabs BC106N-VIS   (c) Thorlabs S314

Fig. 3.7. Selected optical characterization devices for spectral, beam width, and power measurements.
Images obtained from:
https://www.thorlabs.com/thorproduct.cfm?partnumber=CCS175,
https://www.thorlabs.com/thorproduct.cfm?partnumber=BC106N-VIS,
and https://www.thorlabs.com/thorproduct.cfm?partnumber=S314C, respectively.

3.4 System Control

The system is primarily controlled by an NI PXI-8820 running Windows 7 and NI LabVIEW 2014. The LabVIEW virtual instrument (VI) interface continuously reports thermocouple and pressure transducer sensor measurements throughout the system. Temporal sequencing support allows external device timing to millisecond precision. The solenoid valves, pneumatic valve to trigger the flash event, vacuum pump, laser driver, spectrometer, and beam profiler are all controllable through a LabVIEW VI. Sequencing files were written to trigger events and log data as needed for a given set of experimental parameters. For safety, the diode driver has a built in delay period once the signal is given to fire. This timing delay was built in to the sequencing routine and mitigated by turning "ON" with a current of 0 A. To actually fire the laser, the current value is set to a non-zero value. The system is then turned off for safety after completion of a firing event. The main flash CITMAV page shown in Fig. 3.8(a) was modified to include laser diode parameters, while the page shown in Fig. 3.8(b) was created to operate the laser diode driver and spectrometer safely and with maximum experimental flexibility.

3.5 Experimental Procedures

The procedure used to determine experimental runs and characterize the system is discussed next, followed by a detailed description of an experimental run.

3.5.1 Design of experiments

This system includes a number of possible input and output parameters. For this study, the goal is to capture the full mapping between these inputs and outputs in a statistically valid sense, without requiring unreasonable amounts of data collection. In such cases, varying one factor at a time may take too long, and can even create time-dependent biases. Fortunately, an alternative approach that maximizes the amount of
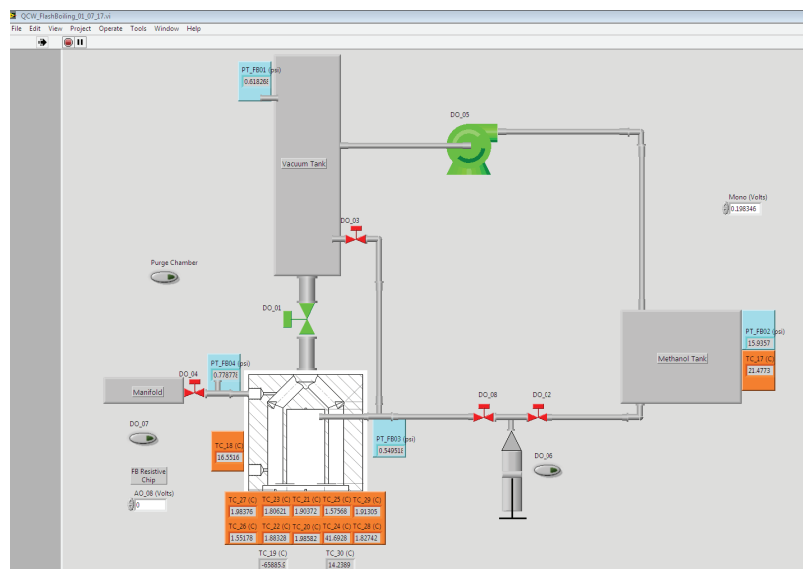
(a) Flash chamber LabVIEW page.
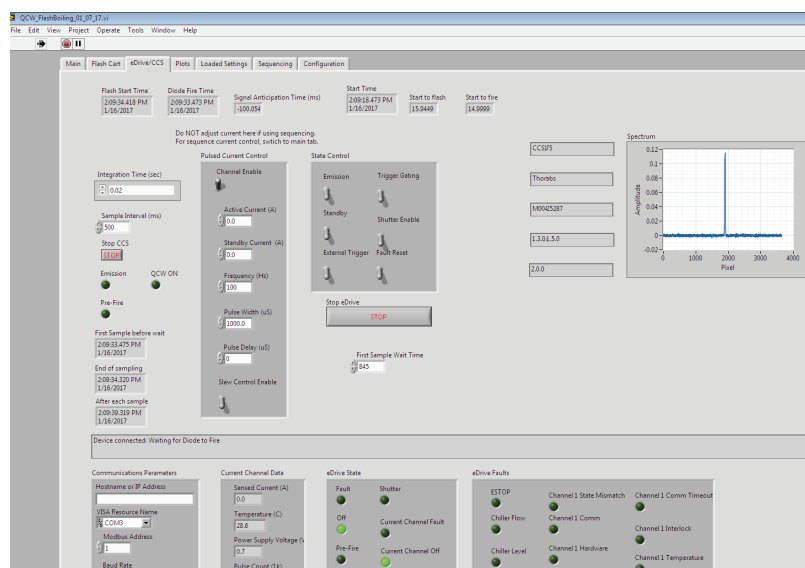
(b) Laser diode and spectrometer page.

Fig. 3.8. Relevant portions of the CITMAV LabVIEW VI responsible for controlling the flash/laser setup.

knowledge generated per run while minimizing biases is possible, known generally as design of experiments (DoX) [71]. Here, Design Expert (StatEase) software is used to define the required number of runs for a two-level (high-low) factorial DoX, generate

statistical surrogate models, and to quantify the variable and output interactions and uncertainties. The primary input variables of interest are current amplitude, anticipation time (difference in time between activation of flash cooling and the lasing event), and volume of methanol. The main outputs of interest are spectrum center wavelength, full width at half maximum (FWHM), and beam quality. The spectral responses are shown after 5 seconds of lasing when the system has typically thermally stabilized; the beam quality measurements are averaged over the course of each test condition to account for variance between pulses and images.

The comprehensiveness of steps between runs combined with computer automation and random sequencing is used to keep test conditions as consistent as possible, while minimizing bias. Meaningful comparisons among test results allow characterization of the system and evaluation of flash boiling as a cooling solution for high-power laser diode bars.

3.5.2 Run sequence

To ensure consistency and uniformity between runs, several prescribed steps must be followed between flash events. First, before any testing commences, helium is forced through the entire system (other than the methanol reservoir) to purge any air or remaining methanol vapors out of the tubing. The vacuum pump is then turned on; once the chamber is pumped down to approximately 0.7 kPa, a purging sequence is initiated. Helium flows into the flash chamber for one second through a solenoid valve. Once this valve closes, another opens to pump the chamber down to vacuum for another second. This cycle repeats 10 times before each experimental run. Once the purging process completes, the desired amount of methanol can be manually withdrawn from the reservoir using the syringe. The vacuum will draw the methanol into the flash chamber, which is followed by a quick burst of helium that brings the flash chamber pressure to approximately 160 kPa to ensure that no boiling or evaporation will occur before the run sequence commences. The vacuum

pump is then isolated from the vacuum tank to maintain a constant system volume throughout the test.

For each measurement run, the desired sequence is selected in the LabVIEW VI. After achieving a target diode temperature, the program triggers the flash event by activating the pneumatic valve before the laser fires in the case of positive anticipation time, and afterwards in the case of negative anticipation time. Spectral measurements are synchronized with the laser start time, and occur every 500 ms for the course of the laser firing (˜5 seconds). Beam images are taken on a different computer. Thermocouple and pressure transducer data are logged throughout the sequence. After the LabVIEW sequence completes, any remaining methanol is burned off by manually triggering another flash event. The purge routine must be completed before reloading methanol and pumping down the vacuum chamber.

4. RESULTS

In this work, DoX is employed for each set of spectral measurements. Statistical surrogate models are then generated from the DoX run results, which provide insight into parameter interactions and output behavior. A more complete understanding of the system physics is achieved through a progression of steps, which begin with preliminary testing, to screening DoX runs, to final runs and model generation. Before taking data, it is hypothesized that an increase in current (power) levels will have a negative linear relationship with beam quality and a positive linear relationship with spectral shift and broadening, as excess heating will increase at higher input power levels. This prediction can be quantified using a very simple model, in which the equilibrium temperature difference ΔT reflects an energy balance between waste heat and temperature flow through the laser system, given by $\Delta T = \frac{L}{kA}[P_{in} - \eta * (P_{in} - P_{thr})]$ when above threshold, where L is the length, A is the cross-sectional area, k is the effective thermal conductivity, η is the slope efficiency, and P_{in} and P_{thr} are the laser input and threshold powers, respectively.

4.1 Individual Run Analysis

Before characterizing the entirety of the system, the effects of individual experimental input parameters were analyzed to help determine the experimental bounds for later tests. The following figures show spectral responses using a slightly damaged diode bar, causing it to produce more waste heat and accentuate the effects on the output variables under consideration. While only the current is explicitly specified for each condition, the total input power can be estimated as the product of the current, the duty cycle, and the diode voltage (approximately 2 V, according to the device datasheet).

Varying the current level displays the greatest correlation of temperature change in the diode emitters with spectral shift and broadening. Fig. 4.1 shows the effects with methanol volume, anticipation time, and duty cycle held constant. At the 20 A level, significant blue-shift occurs and the FWHM narrows as the diode bar rapidly cools over the course of the run. The 60 A run is nearly the ideal operating condition; virtually no shift in central wavelength, and the FWHM is still at the design specification. At the highest power of 100 A, the central wavelength red-shifts nearly 4 nm from the specified design wavelength of 808 nm. However, over the course of the run, the wavelength remains stable. A larger FWHM is also observed.
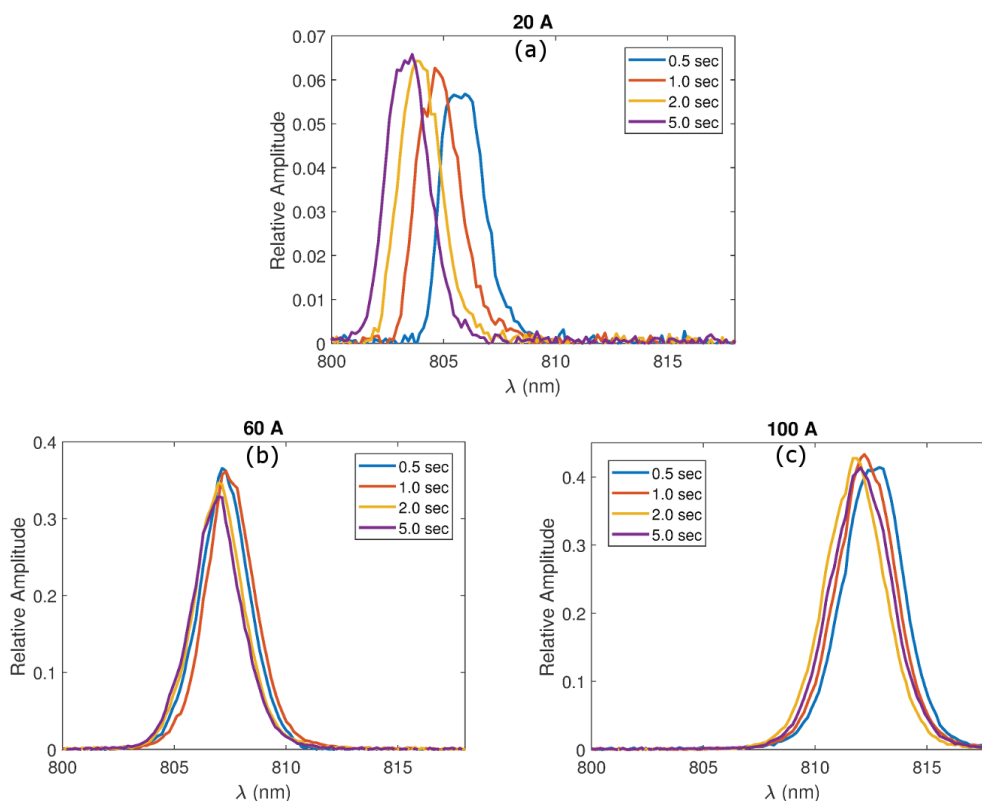
Fig. 4.1. Spectral responses for varying currents with 150 Hz (15% Duty Cycle), 1 mL, +250 ms. Blue-shift is observed in (a), with a final wavelength of 803.6 nm and FWHM of 2.2 nm. (b) is stable with a final wavelength of 807.0 nm and a FWHM of 2.5 nm. The highest current of 100 A in (c) exhibits red-shift, with a final wavelength of 812.0 nm and a FWHM of 3.2 nm.

Variation of anticipation time facilitates the study of diode pre-cooling, as shown in Fig. 4.2. In the -300 ms case, the diode is turned on 300 ms before the flash event begins, while in the +1000 ms case, the diode is cooled for a full second before the laser turns on. The resulting change in central wavelength and FWHM after 5 seconds of measurements is minor, but the shift over time is notably different.

(c)
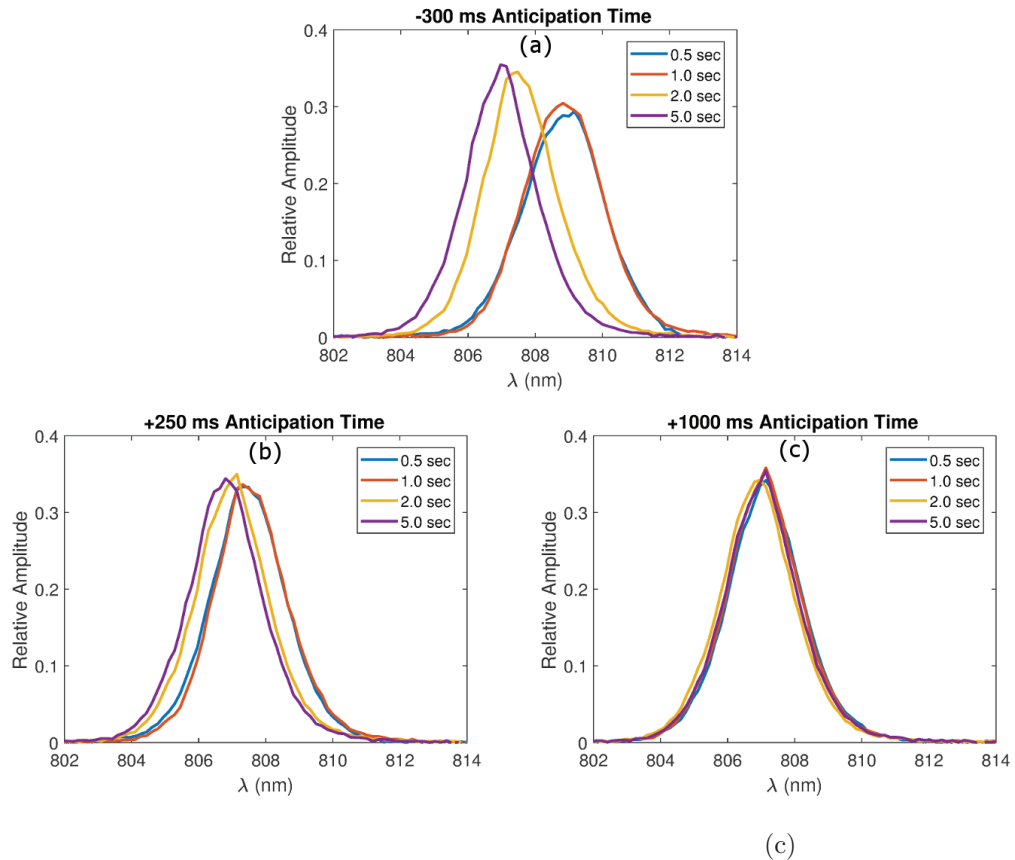
Fig. 4.2. Spectral responses for varying anticipation times with 150 Hz (15% Duty Cycle), 1 mL, 60 A. Initial red-shift is observed in (a) before blue-shifting once the flash event occurs, with a starting wavelength of 809.2 nm, a final wavelength of 807.0 nm, and FWHM of 2.3 nm. (b) is initially stable but blue-shifts slightly, with a starting wavelength of 807.5 nm, a final wavelength of 806.8 nm and a FWHM of 2.4 nm. The longest anticipation time of 1000 ms in (c) is extremely stable, with a starting and final wavelength of 807.1 nm and a FWHM of 2.3 nm.

Varying the amount of methanol yields a counter-intuitive result: flash cooling performs better with smaller volumes of methanol (1 mL). Of course, greater methanol volumes provide greater total cooling capacity, but they also raise the average pressure when flashing, which slows the effect and reduces overall cooling for short time periods. The effect is further explored in the DoX runs discussed later. Fig. 4.3 contrasts the effects of methanol volumes of 1 mL with 4 mL, with the former showing clear outperformance (in terms of the average operating temperature over 5 seconds).
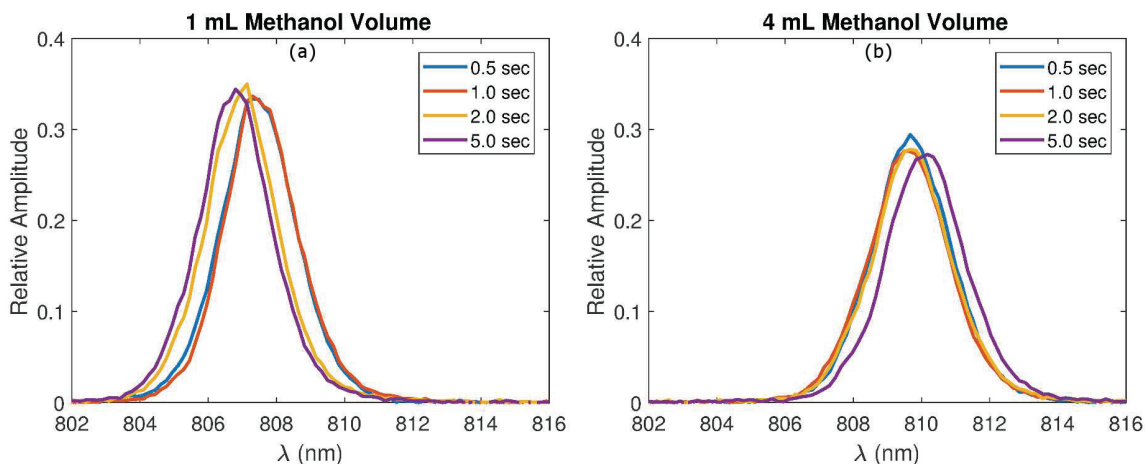
Fig. 4.3. Spectral responses for varying methanol volumes with 150 Hz (15% Duty Cycle), 60 A, +250 ms. For the lowest methanol volume of 1 mL shown in (a), both the final wavelength of 806.8 nm and FWHM of 2.4 nm outperform the 4-mL case shown in (b), where the final wavelength of 810.2 nm and a FWHM of 2.7 nm are noticeably larger.

Consistency and repeatability are important criteria in evaluating nearly any kind of experimental setup. Fig. 4.4 shows three runs with identical input parameters, all from the same series of runs. While there is some slight variance in the initial central wavelengths due to mild inconsistency in the diode driver turn-on sequence, after 5 seconds the final wavelengths and FWHM are in strong agreement for all runs. The amplitudes are also consistent, although relative amplitude data is not considered in DoX analysis. Minor differences in amplitude are due to the pulse averaging

process. Due to differences in repetition rates and pulse widths, it is possible that the occasional sample may have one fewer pulse than the others. The spectrometer integration time is 20 ms unless otherwise specified. Note that individual pulse sampling did not noticeably change the spectral output because the pulse length is relatively long.
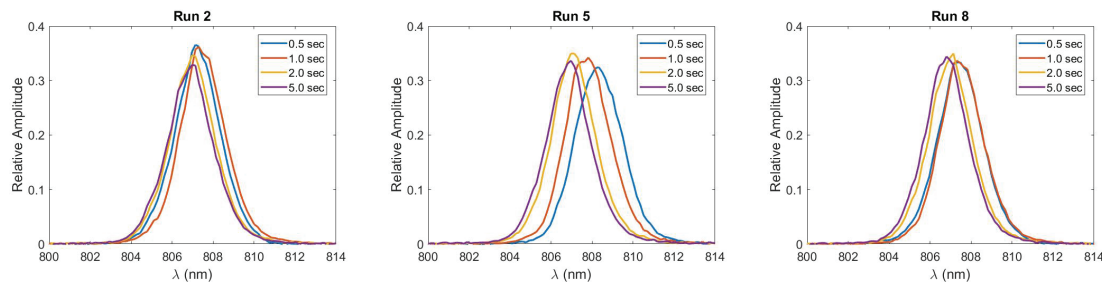
Fig. 4.4. Repeatability for three runs in the same experimental series of runs. Run 2 has a final wavelength of 807.0 nm and FWHM of 2.5 nm. Run 5 has a final wavelength of 807.0 nm and a FWHM of 2.4 nm. Run 8 has a final wavelength of 806.8 nm and a FWHM of 2.4 nm. These values are within the margin of error of the spectrometer.

4.2   First Design of Experiments

The first DoX was intended to screen the system to provide a baseline characterization, setting the stage for further analysis. Based on the initial results, the following ranges of experimental parameters were chosen: diode current (20 to 100 A), anticipation time (-100 to 1000 ms), methanol volume (2 to 4 mL), and frequency (100 Hz or 10% duty cycle). Only spectral shift and broadening are considered here, as the beam quality measurements were not yet implemented at this stage. Two key conclusions were reached in this phase. First, it is possible to substantially raise the optical power output of the diode by increasing the repetition rate (frequency). Second, the response curve for spectral shift of the system, shown in Fig. 4.5, strongly supports the surprising preliminary finding above that lower volumes of methanol in fact *bene-*

fit this transient cooling process. Table 4.1 shows the normalized coded variables for the peak wavelength and spread relationships in the first complete DoX. Normalized coded variables vary from -1 to 1 and represent the minimum and maximum values, respectively, that the parameter can have for a given experiment. For example, in this case, a coded variable of 1 for methanol volume is equivalent to 4 mL of methanol volume. The purpose of these variables is to remove the dimensionality dependence to better identify the relative impact that each factor has on a given output. The adjusted R^2 is the fraction of unexplained variance, adjusted for the number of predictors in the model (penalizes over-fitting), while the predicted R^2 quantifies how well the model predicts responses for new observations [71]. One can infer reasonable agreement between the adjusted and predicted R^2 if they differ by less than 0.2, as stated in the DoX software.
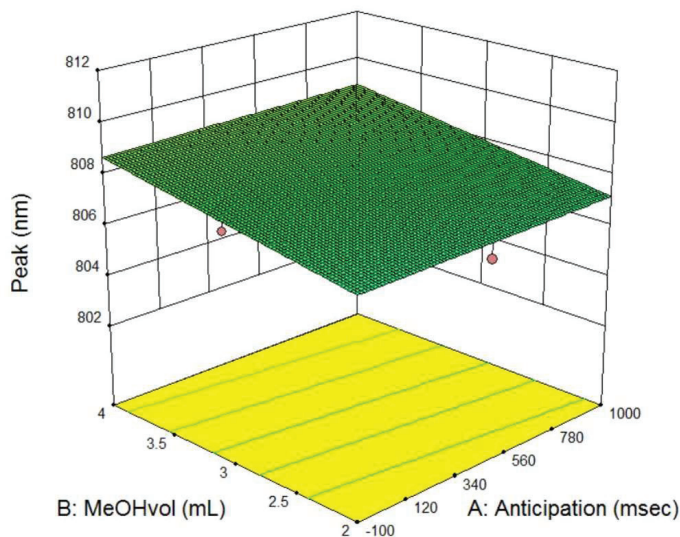
Fig. 4.5. Response surface for the first DoX run at 60 A, showing the correlation between smaller methanol volumes and smaller red-shift.

Table 4.1.
First DoX surrogate model. Normalized coded variables:
A = Anticipation Time, B = Volume Methanol, C = Current.

Equation	Adjusted R^2	Predicted R^2
Peak Wavelength [nm] = +807.94 +0.11*A +0.87*B +3.07*C	0.976	0.964
FWHM (Spread) [nm] = +2.27 +9.3E-3*A -0.045*B +0.7*C	0.946	0.918

4.3 Second Design of Experiments

The first DoX above was then revised to produce a second screening DoX at 50% higher average power, or a frequency of 150 Hz (duty cycle of 15% with 1 ms pulse width). The anticipation time range was extended to (-300 to 1000 ms) to further explore negative anticipation time without risking damage to the diode. Finally, the methanol volume range was shifted to 1 to 2 mL to explore the benefits of lower methanol amounts on cooling, while retaining sufficient volume to avoid dry out.

Fig. 4.6 shows the surrogate model predictions as compared to actual experimental data. Both linear and quadratic models have adjusted and predicted $R^2 > 0.98$ for the spectral shift, while the linear model for spectral broadening has both of those values above 0.94. $R^2 > 0.9$ indicates that the surrogate model developed here is reliable. Furthermore, the trends of this model are consistent with the physical understanding of the system, manifested in a linear increase in wavelength with input power and higher methanol volume. Table 4.2 shows the normalized coded variable surrogate model for the second series of experiments.
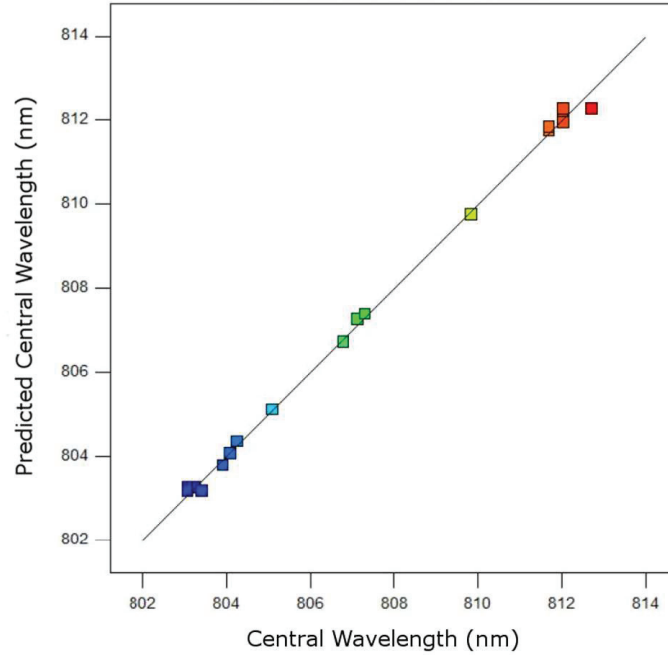
Fig. 4.6. Predicted vs actual experimental points for the second DoX surrogate model for central wavelength.

Table 4.2.
First DoX surrogate model. Normalized coded variables:
A = Anticipation Time, B = Volume Methanol, C = Current.

Equation	Adjusted R^2	Predicted R^2
Peak Wavelength [nm] = +807.67 +0.04*A +0.32*B +4.17*C	0.990	0.985
FWHM (Spread) [nm] = +2.56 +5.1E-3*A +4.33E-3*B +0.59*C	0.962	0.941

4.4   Final Design of Experiments

While the second DoX surrogate model predicts ideal testing parameters consistent with the physical understanding of the system, further improvements and

enhancements are made to obtain a more complete analysis. First, preliminary power measurements at moderate to high power levels with a pyroelectric energy meter indicate that the original diode bar tested exhibits an optical efficiency of 10%, although something in the range of 20-30% is expected, given optical coupling and electrical losses in the system. This means the diode generates excess heat, and therefore optical performance could be greatly improved by replacing the diode bar. Some of this damage may have been caused by clamping wires to the setup, which may have scratched or cracked the diode bar. An improved mount design was implemented in this stage, to ensure that the diode bar remains in a fixed position with high-quality electrical contact, as shown in Fig. 3.5.

Furthermore, at this stage, beam quality was implemented as a new DoX output parameter by adding a beam profiler to the setup, discussed in Section 3.3.2. Fig. 4.7a shows a full raw 3D intensity plot, while Fig. 4.7b shows the calculated transverse y profile, sampled from a test run.
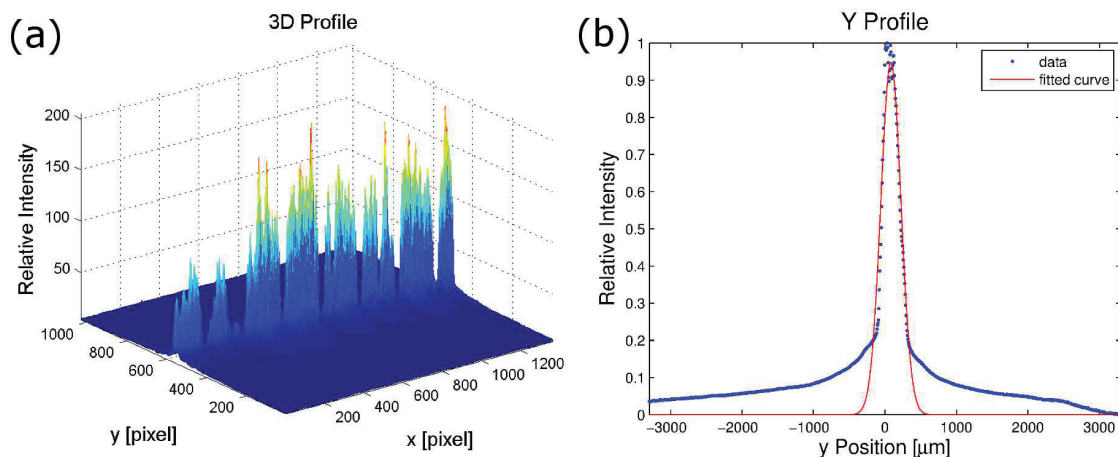
Fig. 4.7. 3D intensity plot (a) and y-profile with 1-term Gaussian fit (b) for the waist measurement of final DoX run 4. Run parameters are 265 ms anticipation time, 2 mL methanol, and 20 A diode current.

Since measurements at two distances are required (one at the waist, one in the far-field), the full set of DoX runs was repeated after this change. While time-consuming,

this approach provides an opportunity to compare spectral outputs and to evaluate the system consistency. The results from the second DoX run suggest the experimental bounds on the input parameters are well-defined. A minor adjustment to the minimum anticipation time seems appropriate, as -300 ms did not show any notable effects and risks overheating the diode. Therefore, the third DoX run adjusted the anticipation time range as 0 to 1000 ms. A 15% duty cycle is maintained. Discrete current levels of 20, 60, and 100 A are used to avoid excessive adjustment of the beam profiler filter setup. Methanol volume is maintained from 1 to 2 mL. Table 4.3 shows the normalized coefficient equations generated by the surrogate model, while Fig. 4.8 shows response surfaces for each DoX output, as well as the relationship between diode current and beam quality. For the center wavelength output, both the quadratic and linear models have high R^2 values; however, based on the simple physical model, the linear model is presented here. Anticipation time has very minimal effect on the final peak and spreads. Again, larger methanol volume corresponds with greater spectral shift and broadening. Current maintains the largest impact, as expected. The beam quality model is not as strong as the spectral shift and spectral broadening models based on the adjusted and predicted R^2. Further discussion of the beam quality model is provided in Section 4.6.

4.5 Power Measurements

Power measurements are taken with the goal of analyzing the optical conversion efficiency of the system, which is estimated as the measured diode output power divided by the total average input power [28]. However, not all losses occur in the laser diode itself; there are also losses from the electrical wiring, contacts, and short current pulse transients (mainly for pulse widths below 500 μs). In addition, even though both optical meters are placed as closely as possible to the diode bar, and theoretically are wide enough, optical coupling losses remain. Furthermore, these losses are accentuated on the higher current runs as the decline in beam quality causes further

Table 4.3.
Final DoX surrogate model. Normalized coded variables:
A = Anticipation Time, B = Volume Methanol, C = Current.

Equation	Adjusted R^2	Predicted R^2
Peak Wavelength [nm] = +806.2 +0.024*A +0.42*B +2.41*C	0.972	0.964
FWHM (Spread) [nm] = +2.17 +0.027*A +0.080*B +0.58*C	0.958	0.944
Beam Quality [M^2] = +95.38 -0.86*A +2.30*B +12.38*C -3.26*AB -0.24*AC +2.17*BC +3.93*A^2 -0.67*B^2 -14.39*C^2	0.914	0.784

beam spreading and coupling losses. Despite these inaccuracies, comparisons across significantly different input conditions and similar current conditions still provide useful trend information. Next, the magnitude of the resulting errors is estimated.

Initial measurements for frequencies at 30 Hz show the thermal meter reads approximately 5-10% higher than the pyroelectric sensor, which is reasonable given the greater coupling losses present in the pyroelectric sensor due to the smaller detector size. The thermal sensor is used for the remainder of the measurements since it can handle higher power levels and is not subject to the 30 Hz frequency (repetition rate) limit. Table 4.4 shows a variety of measurements taken across different power levels using the thermal sensor. Power measurements vary only slightly over time after the initial ˜1 sec delay, caused by the thermal time constant associated with the heat capacity of the detector. Some runs are performed without cooling, so that the efficiency can be compared with or without the flash event. In the cases that the flash occurs, 1 mL of methanol and 1000 ms anticipation time are used, while the laser is fired for 5 seconds. The input power is estimated by multiplying the duty cycle, input current, and diode voltage of 2 V (based on the datasheet specification, this
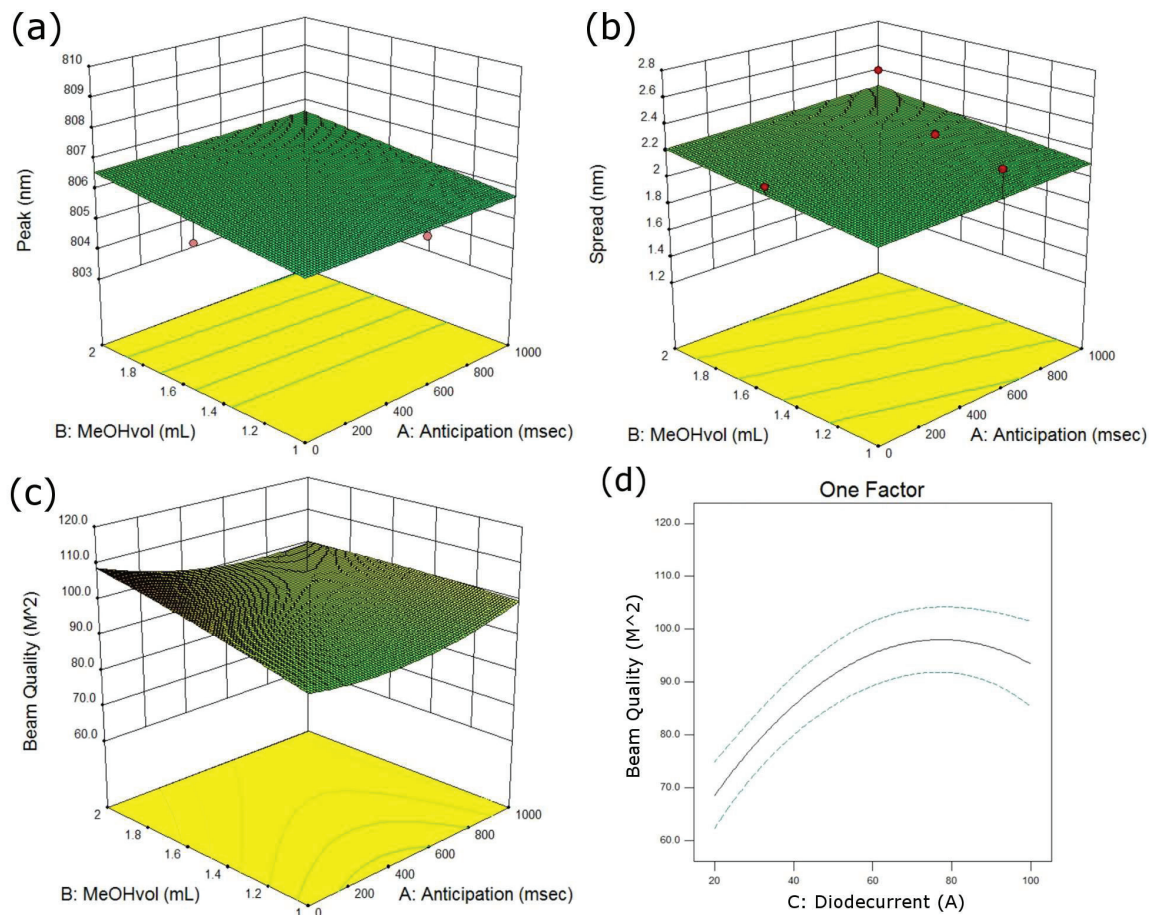
Fig. 4.8. The peak response in (a) and the spread (FWHM) response shown in (b) both demonstrate a positive correlation with the volume of methanol. The beam quality shown in (c) also improves with lower methanol volumes at lower anticipation times, but is insensitive to methanol volume at higher anticipation times. Diode current displays a unique quadratic relationship with beam quality in (d).

slightly overestimates input power as diode voltage is typically under 2 V). Runs 2, 8, and 11 have the same power-related parameters as runs in the final DoX.

Fig. 4.9 illustrates the power and efficiency data from Table 4.4. The order from left to right matches the runs from top to bottom of Table 4.4. There are four main takeaways that can be observed from the plot:

1. Losses due to short pulse transients are observed in runs 4 and 5, which have identical input powers. Run 4 has twice the frequency (repetition rate) with pulse widths half those of run 5, and a resulting observed smaller efficiency. This validates the decision to perform DoX runs with a 1000 ms pulse width.

2. The general increase in efficiency at higher current levels (see Fig. 3.4) can be observed by comparing the 20 A (runs 1-2), 25 A (runs 3-6), 60 A (runs 7-8), and 100 A (runs 9-11) cases. Despite certain system losses, the efficiency *trend* is verified.

3. Even at relatively low power levels, the flash cooling improves device efficiency. Runs 5 and 6 have identical input parameters, but the efficiency is improved for run 6, which has cooling, where run 5 does not.

4. Efficiency is maintained well at high power levels (under 1.5% absolute change). For instance, run 9 with no cooling and an input power of 2.1 W has an efficiency of 25.7%, while run 11 with cooling and an input power of 30 W has an efficiency of 24.3%.

The simple analytical model predicts that the overall efficiency will increase past the diode lasing threshold of ~15 A, asymptotically approaching the slope efficiency of the laser. This relationship is easily observed when comparing the 20 A cases to the higher current cases in Table 4.4. According to the device datasheet efficiency curve shown in Fig. 3.4, the diode efficiency is approximately the same at 60 A and 100 A, independent of temperature. While slight declines in efficiency are generally observed as the duty cycle increases, these decreases are minor, indicating the flash process cools the diode bar to maintain a stable temperature. The thermal power meter can track power over time; its time constant is on the order of 1 second, yet no significant variations in optical power are observed in the five seconds after the initial reading is made. This again indicates stable optical output.

Table 4.4.
Efficiency (η) measurements for a variety of current levels, frequencies, pulse widths, and cooling levels.

Run	Current (A)	Frequency (Hz)	Pulse Width (μs)	Duty (%)	Cooling	Optical Power (W)	Input Power (W)	η (%)
1	20	30	350	1.05	No	0.038	0.42	9.0
2	20	150	1000	15	Yes	0.700	6.0	11.7
3	25	30	350	1.05	No	0.073	0.525	13.9
4	25	60	350	2.1	No	0.144	1.05	13.7
5	25	30	700	2.1	No	0.159	1.05	15.1
6	25	30	700	2.1	Yes	0.170	1.05	16.2
7	60	30	350	1.05	No	0.317	1.26	25.2
8	60	150	1000	15	Yes	4.32	18.0	24.0
9	100	30	350	1.05	No	0.540	2.1	25.7
10	100	30	1000	3	Yes	1.53	6.0	25.5
11	100	150	1000	15	Yes	7.30	30.0	24.3
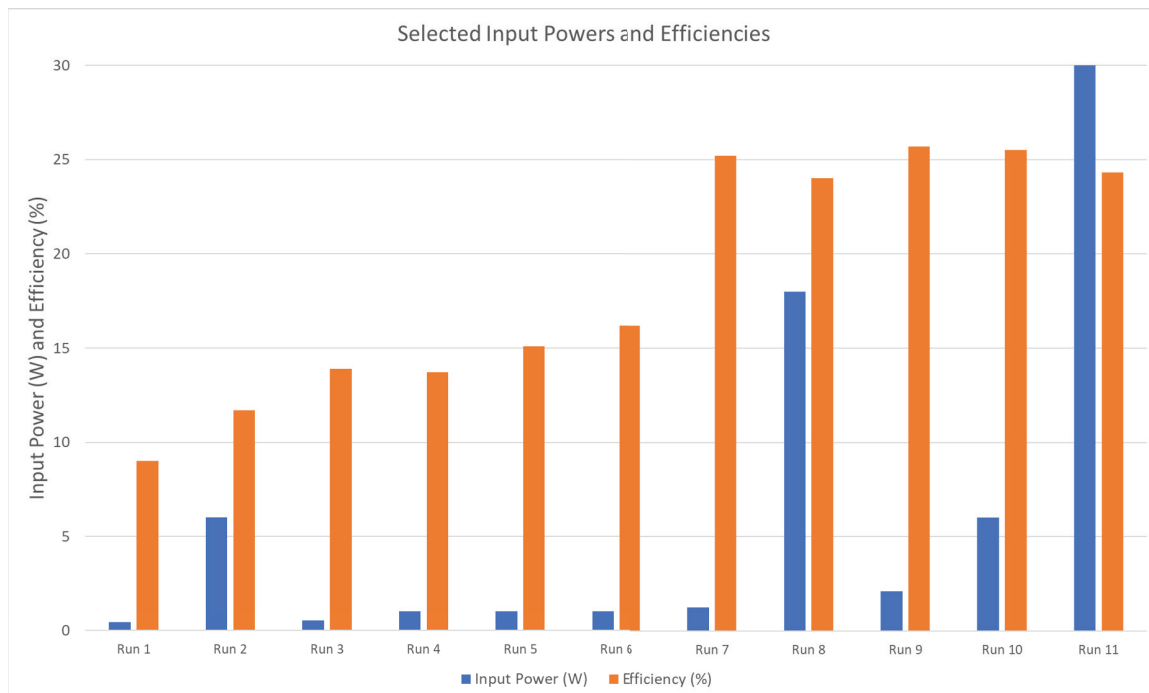
Fig. 4.9. Output power and efficiency plotted for the runs shown in Table 4.4. Current levels generally increase left to right, resulting in the corresponding overall rise in efficiency.

4.6 Discussion

As expected from the analytical models, current is the most important factor in determining the diode bar output characteristics. Varying the current alters the overall input power level, and thus heat generation. The stability of the spectra, even at high current levels, suggests that the transient nature of the flash event overlaps well with the high heat-flux transient heat loads observed in a laser diode bar. Notably, larger initial volumes of methanol negatively impact the transient cooling potential of a flash event, as heat spreader temperature reaches lower values with lower initial volumes of methanol. This initial observation is supported both qualitatively through spectral shift plots, and quantitatively through detailed statistical surrogate models.

For the 20 A case, the flash provides enough cooling power that the emitters drop in temperature over the course of a run, as indicated by a spectral blue-shift. In a real-world application, this spectral shift is likely undesirable but demonstrates the cooling potential of flash boiling in this application. Particularly for the 60 A case (~9 W optical power and waste heat), optical output is stable and maintains the nominal manufacturer specifications listed at a much lower power level (often well under a 0.5% duty cycle). For the 100 A case, minor red-shift is observed, but the peak wavelength is within 2 nm of specifications at room temperature, which is within the rough target application range of 3 nm as a pump source for a Nd:YAG laser. The spectrometer provides a quick and accurate indication of average channel temperature. While a thermocouple is connected to the diode, it is difficult to relate the surface temperature observed at the thermocouple to the change in channel temperature due to the small size of the emitter and temporal discrepancies arising from different time constants in the device. For these reasons, the spectral data provides the most accurate description of channel temperature.

The beam quality calculations produced a surprising result in that beam quality did not degrade linearly with an increase in current (power) levels, as originally hypothesized. A statistically significant increase is observed from the 20 A to the 60 A case, but the 60 A and 100 A cases have similar beam quality values. A plausible explanation for this effect is that thermal saturation occurs within the diode at the higher power levels, resulting in a worst case observed beam quality. Another possibility is that at higher current levels, the beam divergence becomes significant enough to affect coupling to the profiler. The quadratic statistical model shown in Fig. 4.8d likely overfits the region between 60 and 100 A. If experimental data were to be taken within this range, the beam quality would likely remain fairly consistent. While the beam quality measurements require repeating runs, not enough variability exists between runs to explain the observed behavior. Initially, using two profilers in conjunction with another beam splitter was proposed to require only a single run to obtain beam quality data; however, physical and optical system limitations preclude

a full implementation of this method at the present. In addition to this revision of the optics, future work includes fitting the beam quality to an exponential saturation curve or some other non-polynomial function.

While power/efficiency measurements were not integrated into the DoX in real time because of space constraints and optical coupling concerns, separate testing information taken under similar conditions as in the DoX indicates a stable optical output, with trends in efficiency that match a standard laser diode optical efficiency curve. The stability in diode output indicates that flash boiling provides adequate cooling to maintain the diode bar performance, even at high duty cycles.

5. SUMMARY AND RECOMMENDATIONS

Flash boiling is capable of significant rates of heat transfer even for small temperature differences, corresponding to a large effective convective coefficient, and can be triggered when needed nearly instantaneously. The transient nature of a flash event provides a unique counterpart to the high heat flux turn-on regime of a laser diode bar. Here, a vacuum-tight experimental flash rig is combined with a laser diode bar to create an integrated system whose physical behavior is evaluated. Three statistically rigorous set of design of experiments are used to quantify the relationships between anticipation time, volume of methanol, and diode current with spectral shift, spectral broadening, and beam quality. Anticipation time does affect the initial transient behavior and temporal spectral stability, but is found to have little effect on the optical parameters after 5 seconds. Higher performance cooling is found to be achievable with relatively low volumes of methanol, on the order of 1 mL. Of course, smaller amounts of methanol allow for a smaller total level of heat removal, so balancing the amount is an important design consideration. As expected, the average input current magnitude (and therefore average power) is the most significant factor affecting spectral shift, spectral broadening, and beam quality. Despite certain optical limitations of the test setup, flash boiling is shown to support sub-nm spectral shift in laser diode bars operating in the QCW regime at high duty cycles up to 15%, which is more than adequate for many DPSSL applications. In addition, very minor decreases in efficiency are observed as the average power levels increase in the diode, indicating that flash boiling provides enough cooling for stable power output, with relatively minor changes in operating wavelength or FWHM over time.

Since the work described was performed, higher power (500 W) laser diodes have become available [40], which might provide a more challenging test of this cooling capability. In future work, developing a new experimental setup specifically to evaluate

multiple diode bars in series would provide more insight into the ultimate capabilities of flash boiling as a cooling source for diode bar lasers at scale. Such a design accommodating more optical beam paths will allow for further exploration of beam quality without the need for repeating runs. It also could support tests of beam combining. Direct comparison with a single-phase cooling for the exact same device and optical setup would help quantify the advantage flash boiling presents in terms of raw cooling power. Evaluating flash boiling for cooling laser diodes in a pumping application for a SSL or fiber laser system would provide further insight into transient effects at a larger system scale.

Part II

GaN HEMT RELIABILITY THERMAL ANALYSIS

6. INTRODUCTION AND BACKGROUND

6.1 Project Introduction

GaN high electron mobility transistors (HEMTs) have rapidly grown in market share in recent years. They are commonly used in RF, amplification, power electronic, and military applications. The core operating principle for a GaN HEMT in itself provides numerous advantages. A traditional FET provides the charge carriers necessary for inversion by doping, which reduces effective carrier mobility. In an AlGaN/GaN HEMT structure, the spontaneous polarization between the AlGaN and GaN layer results in the formation of a two-dimensional electron gas (2DEG) channel without the need for any dopants. This provides a conduction path with extremely high maximum velocities and effective mobilities. There are a number of advantages that make GaN HEMTs so desirable [72]:

- The wide bandgap of 3.4 eV results in high breakdown voltages, which allow for for use of larger drain voltages and therefore high output impedance per watt of RF power for easier matching and lower loss circuits

- Operating voltages of 28 V and higher simplify connectivity with industrial amplifier setups, reducing system costs [73]

- High efficiency operation due to lower on resistance

- Low output capacitance and resistance is ideal for a switching amplifier

- High saturated drift velocity results in high saturation current and power densities

- High electron mobility facilitates operation at very high cutoff frequencies

- High charge carrier density supports high current density, allowing for a decrease in transistor area and higher power densities

These high power densities result in significant thermal management challenges. Joule heating primarily occurs in the 2DEG layer, especially at the gate edge [74]. To address thermal concerns, many GaN HEMTs are manufactured with a SiC substrate, which has a high thermal conductivity that helps reduce peak channel temperatures when coupled with a cooling solution [75].

Even with adequate cooling, the lifetimes of GaN HEMTs are reduced at prolonged high-temperature operation. There are a wide variety of studies on GaN HEMT reliability. However, many studies lack details pertaining to specific failure mechanisms. Better understanding how individual, thermally dependent failure mechanisms affect the lifetime of a device will help evaluate the efficacy of novel cooling technologies. The research discussed here will aid in the evaluation of a novel electronics cooling solution developed by Justin Weibel's group. The cooling technology involves placing microchannels directly on a device package to minimize thermal resistance and improve the heat removal rate using two-phase flow. Background information pertaining to accelerated life testing, failure mechanisms, and reliability modeling techniques is discussed in the rest of this chapter. Details concerning the thermal and reliability modeling of an off-the-shelf GaN HEMT produced by Wolfspeed (a Cree company) are discussed in Chapter 7. Finally, conclusions are presented in Chapter 8.

6.2 Accelerated Life Testing

Because GaN HEMTs can operate at higher temperatures, electric fields, and current densities than many other kinds of transistors, there are a unique set of possible failure mechanisms that can reduce the operating lifetime [76].

There is not much long-term reliability data in real-world use conditions available because GaN is a relatively new technology. Accelerated life testing (ALT) is the alternative, developed over the last several decades by international teams of

researchers spanning multiple application areas. In ALT, tests spanning hundreds or thousands of hours at high stress conditions (commonly temperature or voltage) are extrapolated for potentially millions of operation hours. There are three main considerations for ALT to be a valid approach [77]:

1. GaN devices must have similar diffusion-based failure mechanisms as other semi-conductor devices for which ALT is commonly used. This is a reasonable assumption, as it has been well established that diffusion is the key process for many failure modes in GaN devices [78].

2. ALT needs to accelerate the same failure mechanisms that would occur under normal operation.

3. The channel temperature is a known quantity. This can be approximated with IR imaging techniques combined with finite element method (FEM) modeling.

Thermally induced failures generally follow the Arrhenius model, which is commonly used to model diffusive processes and for semiconductor reliability. The general mean time to failure (MTTF) is related to the peak junction temperature as shown in the following equation:

$$MTTF = Ae^{(E_a)/kT},$$

where A is a model constant, E_a is the thermal activation energy, k is the Boltzmann constant, and T is the junction temperature. This general equation has been modified for the semiconductor failure rate for junction temperature T and voltage V [79]:

$$R(T, V) = R_O(T)V^{\gamma(T)},$$

where $R_O(T)$ is the Arrhenius function of temperature given above and the power dependence γ varies between 1 and 4.5 to account for acceleration due to applied voltage. The activation energy E_a can be calculated from measured mean failure times t_1 and t_2 at two different temperatures T_1 and T_2 as,

$$ln(t_1/t_2) = (E_a)/k(1/T_1 - 1/T_2).$$

The accuracy of the Arrhenius model is highly dependent on uncertainties in activation energies and junction temperature values.

For device lifetime testing, generally only one parameter is varied at a time (usually temperature). Lifetimes are obtained at higher temperature values and extrapolated for cooler temperatures that would require longer testing times. The JEDEC JEP118 publication Guidelines for GaAs MMIC and FET Life Testing serves as a reference for conduction of accelerated life testing. High accuracy of channel temperature estimates and material thermal conductivities is necessary for extrapolation at orders of magnitude greater MTTFs. Generally, RF tests have lower activation energies than DC tests and have shorter MTTFs as a result [80].

Overall, ALT provides optimistic data predictions for GaN HEMT reliability, but there needs to be larger sample sizes and greater transparency in population statistics to achieve greater confidence in the statistical significance of the extrapolated device lifetimes. In addition, testing at channel temperatures significantly higher than general operating conditions may introduce failure mechanisms that would not be experienced under normal operating conditions, and vice versa. The higher temperature failure mechanisms could also mask failure mechanisms that occur at lower activation energies, so longer term testing at lower temperatures could help evaluate the model validity [80]. Finally, while a great deal of industrial reliability testing has been conducted, much of this information, particularly pertaining to specific failure modes, is unavailable. Better modal analysis and more detailed reporting will help predict future device reliability in specific operating regimes. Fig. 6.1 shows a composite Arrhenius plot compiled from many published industry sources. Note that at a given junction temperature, unique devices may have MTTFs differing by over two orders of magnitude.

Fig. 6.2(a) shows the trend (or lack thereof) in E_a over time, which highlights the variability throughout the industry. Fig. 6.2(b) shows that for a given activation energy, the MTTFs can be orders of magnitude apart due to differences in manufacturing and material quality. In one study, different vendors produced devices with
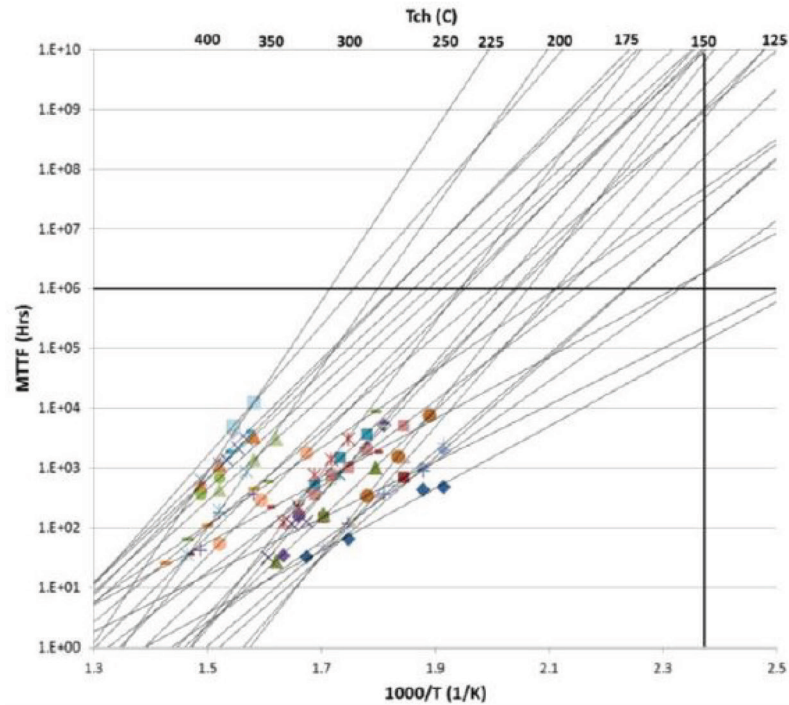
Fig. 6.1. Composite Arrhenius plot for industrial GaN HEMTs [80].

very similar specifications, but one vendor's devices showed over a 32% decrease in peak transconductance after 48 h at 150 ℃, while the other only had a 0.07% decrease [81]. The study concluded that quality of the AlGaN/GaN epitaxial layers on the SiC substrate can strongly affect the reliability of the device.

6.3 Failure Mechanisms

Failure is often defined as a drop of 10-20% or 1 dB of a performance parameter, although this can vary widely over different test protocols. There are three main categories of GaN HEMT failure mechanisms: contact degradation, hot-carriers and trap generation, and the inverse piezoelectric effect. Fig. 6.3 shows general regions where these major failure mechanisms may affect a generic GaN HEMT structure.
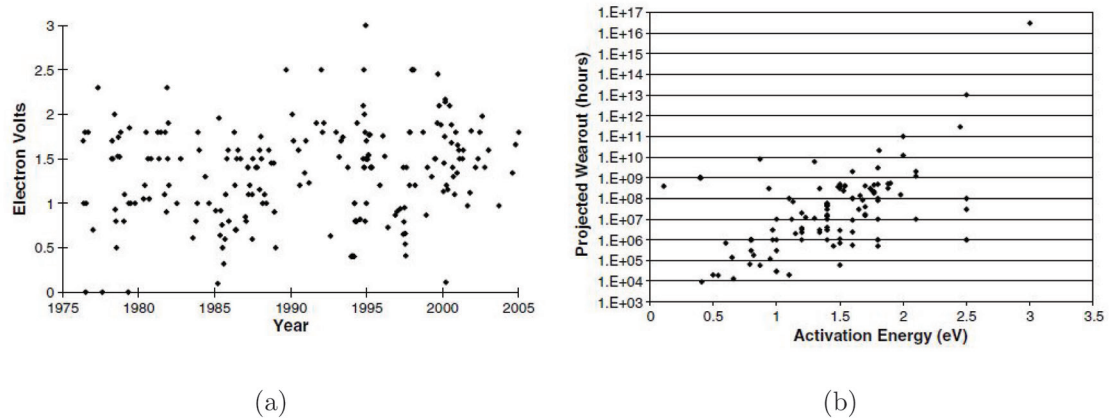
Fig. 6.2. Reported activation energies (a) and relationship of lifetimes to activation energies (b) [75].
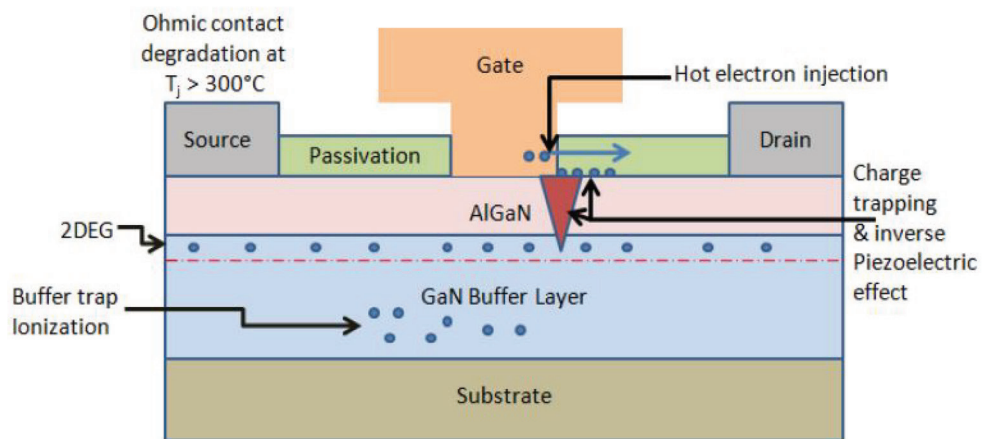
Fig. 6.3. Schematic of degradation mechanisms in AlGaN/GaN HEMTs, including surface pitting, hot electron injection, and contact degradation [79].

Contact degradation is generally not an issue below 400 ℃ [79]. If temperatures were to reach these high levels, diffusion between metal layers and from semiconductor to metal can increase contact resistance, reducing the efficiency and maximum saturated current of the device.

One of the dominant failure mechanisms in GaN HEMTs is the increase in density of deep-level traps. Trap generation at moderate drain bias (<20 V) is due only to hot carriers [82]. At higher drain voltages, the inverse piezoelectric effect and localized hot carrier injection from the gate begin to further enhance degradation. Current collapse and gate lag under high voltage and high current is often due to trapping effects created by hot electrons, which are electrons with high kinetic energy due to acceleration in a strong electric field. Generated hot electrons in the region between the gate and drain are likely to be trapped at the interface between the passivation layer and the AlGaN barrier layer or in the AlGaN barrier layer [81]. Under high V_{DG}, the traps result in an increase in the width of the depletion region between gate and drain. The larger depletion width increases effective drain resistance and therefore the saturated drain-source current I_{DSAT}. The trap formation causes reversible degradation in the transconductance G_m and I_{DSAT}, but damage can become permanent at high enough stress levels [79]. Electroluminescence can be used to observe uniform hot carriers along the channel. Different passivation materials can affect the susceptibility to hot-carrier degradation [81].

The inverse piezoelectric effect describes the vibrational response to an applied electric field in a material. The electric field inside the device induced by high voltage increases tensile stress in the AlGaN layer. If the stress becomes too large, the layer relaxes by forming crystallographic defects. This suggests there is some critical voltage that if exceeded, causes these defects [83]. This is observed by an irreversible sudden rise in reverse bias gate current and the onset of I_{DSAT} and series resistance degradation. Some of the crystal defects behave as electrical traps [79]. If the degradation is severe enough, surface pitting and further electron leakage from the gate may occur. This is an electric field driven effect, and not a current driven effect, although heat from high currents may accelerate degradation in general.

6.4   Individual Failure Mechanism Testing

As of the date of this writing, there is no formal RF GaN reliability standard. With uses spanning from high-voltage to high-current to high-frequency, and differences in manufacturing processes, numerous failure mechanisms and rates are introduced. Industry, government, and academic researchers have a significant amount of reliability data, but much of it is unshared and the tests performed vary widely due to the aforementioned variable applications and designs. Isolating and reporting individual failure modes can help improve overall GaN HEMT reliability by moving towards standard testing procedures for the different failure mechanisms.

In RF semiconductors, it is often the case that there are multiple possible degradation mechanisms that can contribute to the wearout of a device. Many degradation mechanisms depend strongly on applied voltages, so it can be difficult to isolate a failure mechanism in an RF application with varying voltages. Further, temperature plays a key role in not only the rate failures occur, but also in which failure mechanisms are the most dominant. Many groups will perform a set of RF life tests at different operating temperatures until failure of a single parameter. This approach can give an average failure rate and may be appropriate for other types of semiconductors. However, the exact combination and contribution of various failure mechanisms may be unknown, making it difficult to extrapolate an average curve with certainty. Here, a new method developed by Paine, Burnham, Ignacio, et al. from Boeing is discussed that allows for tracking the effects of individual failure mechanisms on device reliability.

The core idea of this approach involves finding "signature parameters", which are easily measurable quantities that indicate degradation via a single failure mechanism. Signature parameters primarily scale with their associated failure mechanism alone and can be used to estimate the thermal activation energy for that specific mechanism [84]. DC experiments are less expensive than RF tests, require shorter times to perform, require simpler equipment and calibrations, and are easier to estimate

channel temperatures via thermal modeling. DC testing does not cover all aspects of reliability, since the bias point is constant over an analysis period. Testing at multiple bias points at a range of temperature can highlight the individual failure mechanisms and determine the activation energies. Tracking signature parameters during a single RF test can then be performed to determine initial RF degradation rates. A scaling factor between the RF and DC cases is a simple ratio of the MTTF in each testing regime. The ratio is constant with temperature if the activation energies and Arrhenius factor is the same under DC and RF cases.

The first step is to identify the relevant signature parameters and associated failure mechanisms. There are three main failure mechanisms characterized here:

1. Surface pitting next to the gate on the drain side appears to result from high gate-drain potential. The associated signature parameter is the change in δI_{dmax} (drain current, measured at low V_d (1 V here)). While stress is applied with large V_{dg}, δI_{dmax} is measured at low I_d to minimize overlap effects with hot-carrier injection.

2. Hot-electron generation of fixed charge between the gate and drain causes local pinch-off. This is observed in the reduction of peak transconductance, δG_{mp} [82]. The zone for peak hot-electron effects was found with electroluminescence measurements.

3. Electron trap generation occurs near the gate and affects the depletion area below the gate. This is apparent through the change in threshold voltage, δV_{th}, without a corresponding change in the gate turn-on voltage δV_{gon}.

Both surface pitting and hot electron damage have a similar end result of irreversible pinch off, which can make distinguishing between the two difficult during DC testing. However, the early stages of degradation occur at different physical locations - surface pitting adjacent to the gate contact on the drain side, while hot electron damage is widely spread between the gate and drain [85]. The initial effects of surface pitting are local depletion spots that block current flow, effectively reducing

the channel width and is observed in maximum drain current changes. Hot electron damage begins across the entire channel width and gradually reduces the effect of the gate, and is best monitored via changes in transconductance. While transconductance changes will be observed in I_{dmax}, the effects can be minimized by measuring I_{dmax} at low drain voltages, where G_{mp} is small but I_{dmax} is relatively large. G_{mp} is then measured at high V_d where it is the most sensitive to changes in the gate drain region [85].

Figure 6.4 shows the biases for different degradation mechanism zones.
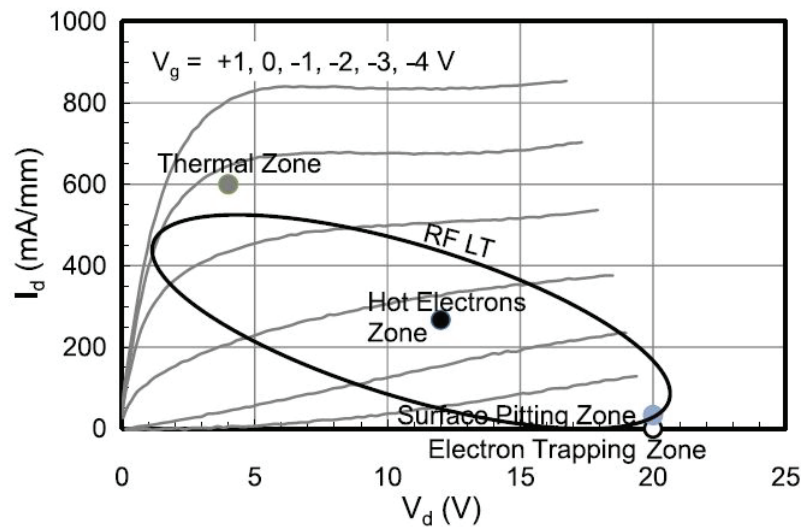
Fig. 6.4. Bias zones targeting each degradation mechanism, compared with typical drain IV curves [86].

Once signature parameters have been established and DC lifetime tests completed, activation energies for each failure mechanism can be extracted. DC lifetests show changes in signature parameters were nearly linear with respect to $\sqrt{time}$, which is common for diffusion-based mechanisms [86]. Fitting this data to an Arrhenius plot gives the thermal activation energy, E_a.

The next step is to relate the failure rates from multiple DC tests to the results of a single RF failure test. RF testing at a single temperature and bias condition for

each signature parameter takes place and is then related to the DC lifetest MTTF. This minimizes the number of complicated and often expensive RF tests required. A scaling constant is generated as a simple ratio between the DC and RF lifetimes, independent of time or temperature. The end result is that the DC MTTFs can be multiplied by the scaling constant to estimate the RF MTTFs. The major key assumptions necessary in relating DC to RF lifetime testing are discussed below [87]:

- In both DC and RF testing, each signature parameter scales only with its associated degradation mechanism and does not affect other mechanisms. Experimental results indicate this assumption is valid up to 10% degradation in DC parameters or a 1 dB decrease in RF gain, so it is valid for early stages of degradation. The assumption is easily justified in the DC case, since the exact failure mechanisms can be biased into a dominant state. For the RF case, because failure mechanisms generally alter a signature parameter in the same direction, any cross effects would result in a shorter MTTF, or a more conservative estimation.

- In RF operation, the only degradation mechanisms that occur are those observed during DC testing. This is reasonable for small levels of degradation, as each failure mechanism manifests physically at different locations. Any acceleration between mechanisms is captured in the scaling constant. This assumption has been validated by RF testing at more than one temperature and accounting for uncertainties in any minor changes in activation energies.

- The scaling factor is a constant and is independent of temperature. This is valid for small degradation in the DC case and for the RF case if the input power is adjusted to ensure that the degree of output compression does not vary.

In combination with some other minor assumptions, this method overall results in an uncertainty in MTTF of approximately -35% and +100% for the lower and upper bounds, respectively. The technique works better for high performance parts with established good reliability, so a commercially manufactured device from a well-known

manufacturer is a good candidate. Fig. 6.5 shows the results of scaling individual failure mechanisms from an RF test. At higher temperatures, surface pitting will usually cause failure before hot carrier injection, unless high quality manufacturing practices minimize the development of surface pitting [85].
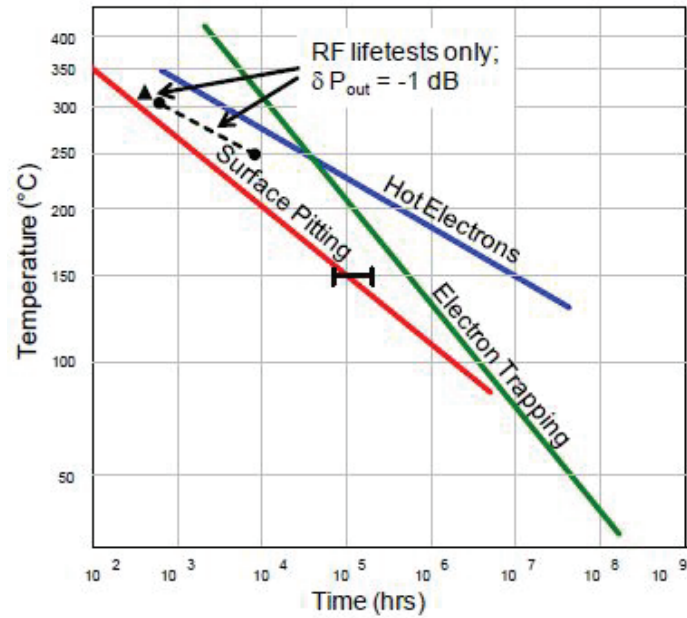
Fig. 6.5. Arrhenius plots for various failure mechanisms, measured in an RF lifetest [87].

7. MODELING APPROACH AND PRELIMINARY RESULTS

The experimental portion of this project will begin with testing off-the-shelf Cree Inc. GaN HEMT devices. The goal will be to isolate and characterize individual failure mechanisms using ALT. Once preliminary characterization is completed, the impact of new cooling techniques on device reliability can be evaluated.

Cree has published a few papers concerning reliability, life testing, and modeling for some of their most popular GaN HEMTs. Much of the reliability data is withheld, but building off their approach and incorporating the techniques from Section 6.4 will provide a strong starting point for characterizing off-the-shelf devices. Results from Cree are discussed along with the development of a thermal model and connected reliability model.

Due to the high-power densities present in GaN HEMT devices, thermal modeling is important to determine the channel temperatures under operation. Like all semiconductor devices, GaN HEMT device reliability is directly proportional to peak channel temperature. A finite element method (FEM) model can be used to solve steady-state heat diffusion equations by discretization of a body into smaller regions or elements. Algebraic equations approximating the solution are generated and solved at the boundaries of the elements, resulting in an temperature profile for the body limited in accuracy by the resolution of the spatial discretization [88].

The following describes the modeling approach used by Cree, detailed in [89]. Ansys® is a commonly used tool for performing the FEM analysis. Using this software, Cree models the device with a fixed boundary condition of 75 ℃ at the device fixture. The heat source is treated as a 0.4 µm source, which is the gate length for the G28V3 line. Thermal analysis can be calibrated by using a temperature-controlled heat sink and characterizing via IR microscopy. Thermal resistance is calculated by

dividing the difference in temperature between the channel and the case (packaging) by the dissipated power. Since the IR images are spatially averaged in high heat flux areas, statistical techniques are applied to estimate the uncertainty in the measurements. The full channel length is averaged in the FEM model (~7 μm) to compare with the IR data (~7 μm resolution). If the averaged model data falls within a 95% confidence interval of the IR data, then model is considered accurate and the peak channel temperature from the FEM model can be used. A thermocouple attached to the device package provides an accessible temperature reading that is then related to the peak channel temperature by the FEM model, eliminating the need for repeated IR measurements. Fig. 7.1 shows a cross section of the gate area for a G28V3 device with a 0.4 μm gate length. An Ansys® model was created from the specifications given in [89] because Cree does not provide access to the model. Fig. 7.2 shows the 2D FEM model re-creation after it has been meshed and solved for an arbitrary heat load. The model provides maximum tuning flexibility for any future modifications.
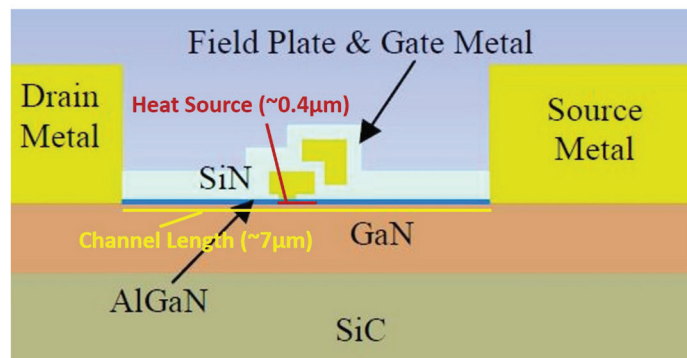
Fig. 7.1. Cross section of gate area for a Cree GaN HEMT showing SiC, GaN, AlGaN, Gate and Drain/Source Metals, Field Plate and SiN. Adapted from [89].

In addition to the modeling approach, Cree also details some reliability results [90, 91]. Reliability is extremely important for Cree because their GaN devices have many applications including military (communications, counter improvised explosive device systems, and radar), civil, industrial, scientific, and wireless (4G, LTE, WiMAX). The
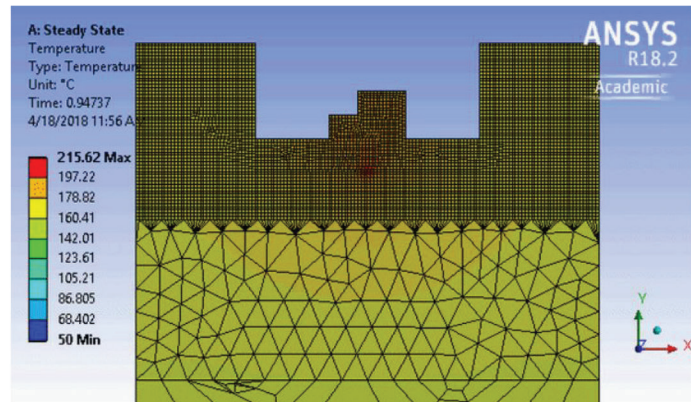
Fig. 7.2. 2D steady-state Ansys® model, reproduced with information from [89].

G28V3 line has been produced at mass scale for over a decade and features a SiC substrate.

For reliability analysis, the channel temperature is estimated as the maximum junction temperature in the channel just under the drain side gate corner. DC ALT were performed at 28 V DC, 6 W/mm, and up to 380 ℃ maximum junction temperature. Failure is determined either by a catastrophic failure event or a 1 dB decrease in saturated power. The Arrhenius fit yields an activation energy of 1.8 eV for 3" wafers and 1.6 eV for 100 mm wafers, and lifetimes on the order of approximately 10^4 - 10^6 hours at junction temperatures of 250 - 300 ℃ [90]. After ALT at 380 ℃ resulting in over a 1 dB degradation in saturated power, Cree observed intermetallic mixing of the ohmic contacts and gold interconnect metal on the source side. There was no evidence of inverse piezo-electric lattice deformation after 28 V ALT. There was also no evidence of gate sinking.

There are a number of types of ALT detailed in [91] for a wider range of Cree products. All tests are done on discrete devices with 3.6 mm gate periphery. A summary of the tests is given here:

- DC-ALT / high temperature operating life (HTOL) is usually performed at the 28-V operating voltage and maximum power density of 6 W/mm. Gate control circuits ensure the current is held constant for the device. The base plate temperature is set and actively controlled to obtain the desired average peak junction temperature, which is determined by relating the temperature reading from a thermocouple attached to the package to the FEM model. ALT is an intrinsic test where the device is stressed for a given time and then run under DC and RF tests. The process is repeated until signs of failure are evident. DC-HTOL is an extrinsic test where the device is run continuously for 1,000 hours and then finally tested at room temperature.

- RF-ALT / HTOL are similar, but performed at RF operating conditions. Cree's tests are done on a reliability test system made by Accel-RF Instruments Corporation.

- High temperature reverse bias (HTRB) involves the continuous exposure of the die and package to the worst case reverse bias (usually 2.5 - 3 times the nominal operating drain voltage) at the maximum recommended case temperature. This test targets high electric field failure modes and defects at the die-level.

A device failure for one of these tests is defined as a condition in which a stressed device has a 1 dB change in critical RF parameters such as small signal gain, saturated power (P_{sat}), or saturated power drain efficiency, a 20% change in saturated drain current or on-resistance, loss of pinch-off gate control, or displays external physical damage [91]. Most failure lifetimes are extrapolated following a $1/\sqrt{time}$ relationship. DC-ALT results in smooth performance changes over time, while RF-ALT begins smoothly and eventually reaches some catastrophic failure time. The DC and RF test procedures yield nearly identical lifetimes at the maximum recommended operating temperatures. In general, at higher temperatures, RF will cause failure first, while at lower more realistic operating temperatures, DC causes failure first. Fig. 7.3 shows

the results of the reliability testing for four of Cree's most popular GaN HEMT product lines.
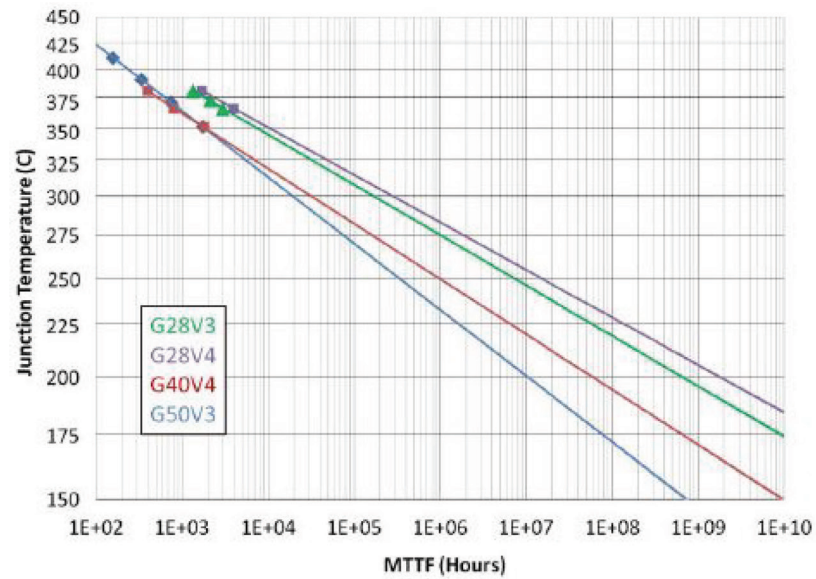
Fig. 7.3. Cree reliability information for popular GaN HEMT product lines. Median time to failure and intrinsic lifetime extrapolations for G28V3, G28V4, and G40V4 DC-ALT, and G50V3 RF-ALT [91].

After developing the Ansys® model for a G28V3 device, a MATLAB program was developed to model device failure with the Arrhenius method. The program can simulate device failures with inputted E_a, V, or temperature ranges. The program can also import .txt files exported from the Ansys® model containing channel temperatures. Failure lifetimes as a function of coldplate temperature or other cooling parameters such as convective coefficient or coolant temperature can be calculated with respect to mean or peak channel temperatures. As with the FEM model, the MATLAB program is designed to be as flexible as possible so that experimental data can easily be incorporated. Multiple activation energies and combinations are possible. Fig. 7.4 shows sample Arrhenius plots that emphasize the effects of varied voltage and activation energies. Fig. 7.5 shows the result of varying coldplate temperature in the Ansys® model for the Cree G28V3 device.
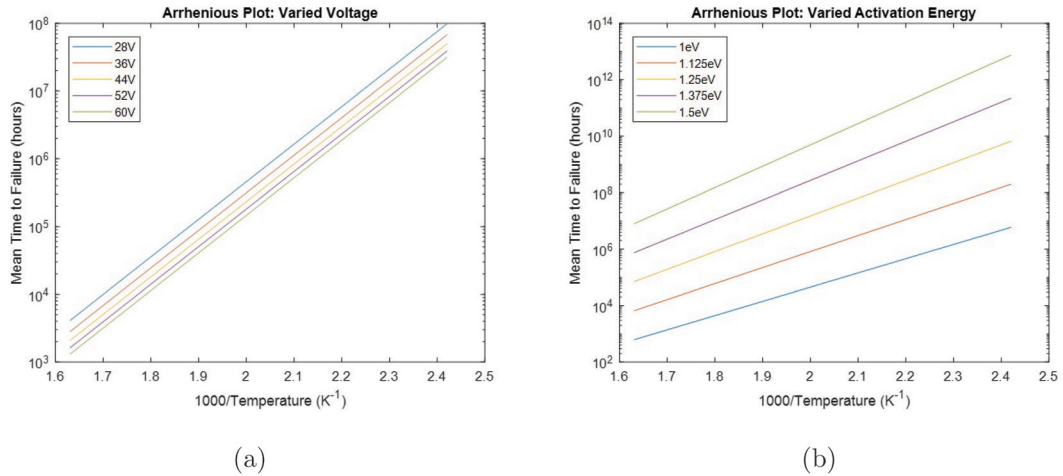
Fig. 7.4. Sample MATLAB program output showing Arrhenius curves as a function of (a) voltage ($E_a = 1.1$ eV) and (b) activation energies (V = 25 V). The junction temperature ranges from 140-340 °C.
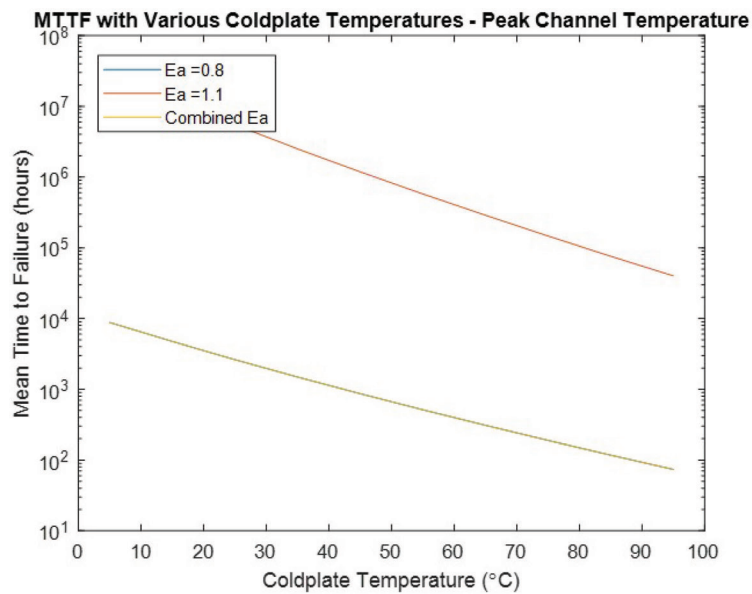
Fig. 7.5. Arrhenius plot for varied coldplate temperatures in the Ansys® model for the Cree G28V3 device. Obviously, a colder coldplate temperature will decrease the junction temperature and increase the MTTF. In this case, the lower E_a of 0.8 eV dominates the combined failure lifetime. These curves are not exactly linearly on the log scale due to the nonlinearities in the conduction coefficients with respect to temperature.

8. SUMMARY AND RECOMMENDATIONS

Here, a literature review concerning GaN HEMT reliability has been used to create a plan for testing off-the-shelf devices. An FEM model has been developed that can be used to predict peak channel temperatures given an input power density and various cooling parameters. Techniques have been discussed that allow isolation of individual failure mechanisms to provide greater detail and insight into GaN HEMT failure modes than what a manufacturer would typically provide. Arrhenius equations can be used to predict device lifetimes based on operating conditions and these specific failure mechanisms. The groundwork performed in this study will provide a starting point for experimental reliability testing of off-the-shelf commercial parts. This testing will coincide with the development of a new cooling technique by Justin Weibel's group. The modeling and reliability analysis described here will enhance the understanding of the long-term impact on reliability of this new cooling approach. As GaN HEMTs continue to grow in both power density and market share, understanding the thermal behavior and its impact on failure mechanisms impacting reliability will continue to be of paramount importance.

The most critical next step will be to begin physically testing devices so that the thermal and Arrhenius model can be fine-tuned for activation energies of the dominant failure mode(s) in the latest devices. Evaluation of the new cooling technique (higher power and/or lower temperature operation) can then be performed once model parameters and uncertainties have been fully established.

REFERENCES

REFERENCES

[1] H. An, C.-L. J. Jiang, Y. Xiong, Q. Zhang, A. Inyang, J. Felder, A. Lewin, R. Roff, S. Heinemann, B. Schmidt, and G. Treusch, "Advancements in high-power high-brightness laser bars and single emitters for pumping and direct diode application," in *SPIE LASE.* International Society for Optics and Photonics, 2015, vol. 9348, p. 93480I.

[2] W. Koechner, *Solid-State Laser Engineering*, 6th ed. New York: Springer, 2006, no. 1.

[3] S. J. McNaught, H. Komine, S. B. Weiss, R. Simpson, A. M. Johnson, J. Machan, C. P. Asman, M. Weber, G. C. Jones, M. M. Valley, A. Jankevics, D. Burchman, M. McClellan, J. Sollee, J. Marmo, and H. Injeyan, "100 kW Coherently Combined Slab MOPAs," in *Conference on Lasers and Electro-Optics/International Quantum Electronics Conference.* Washington, D.C.: OSA, 2009, p. CThA1.

[4] R. L. Byer, "Diode LaserPumped Solid-State Lasers," *Science*, vol. 239, no. 4841, pp. 742 LP – 747, feb 1988.

[5] C. Kopp, "High Energy Laser Directed Energy Weapons," pp. 1–1, may 2008.

[6] J. Marmo, H. Injeyan, H. Komine, S. McNaught, J. Machan, and J. Sollee, "Joint high power solid state laser program advancements at Northrop Grumman," D. V. Gapontsev, D. A. Kliner, J. W. Dawson, and K. Tankala, Eds., vol. 7195. International Society for Optics and Photonics, feb 2009, p. 719507.

[7] A. E. Siegman, "How to (Maybe) Measure Laser Beam Quality," in *DPSS (Diode Pumped Solid State) Lasers: Applications and Issues.* Washington, D.C.: OSA, jan 1998, p. MQ1.

[8] M. Voss, C. Lier, U. Menzel, A. Barwolff, and T. Elsaesser, "Time-resolved emission studies of GaAs/AlGaAs laser diode arrays on different heat sinks," *Journal of Applied Physics*, vol. 79, no. 2, p. 1170, 1996.

[9] Y. Varshni, "Temperature dependence of the energy gap in semiconductors," *Physica*, vol. 34, no. 1, pp. 149–154, jan 1967.

[10] C. Eichler, S. S. Schad, M. Seyboth, F. Habel, M. Scherer, S. Miller, A. Weimar, A. Lell, V. Härle, and D. Hofstetter, "Time resolved study of laser diode characteristics during pulsed operation," in *Physica Status Solidi C: Conferences*, vol. 0, no. 7. WILEYVCH Verlag, dec 2003, pp. 2283–2286.

[11] H. Brugger and P. W. Epperlein, "Mapping of local temperatures on mirrors of GaAs/AlGaAs laser diodes," *Applied Physics Letters*, vol. 56, no. 11, pp. 1049–1051, mar 1990.

[12] O. A. Louchev, Y. Urata, M. Yumoto, N. Saito, and S. Wada, "Thermo-optical modeling of high power operation of 2μm codoped Tm,Ho solid-state lasers," *Journal of Applied Physics*, vol. 104, no. 3, p. 033114, aug 2008.

[13] A. Ghadimi and S. Alikhah, "Simulation and analysis of dependence of threshold current and gain of $\lambda/4$ shifted DFB laser through transfer matrix," *Journal of Optics*, vol. 46, no. 4, pp. 479–485, dec 2017.

[14] Z. Yuan, J. Wang, D. Wu, X. Chen, and X. Liu, "Study of steady and transient thermal behavior of high power semiconductor lasers," in *2009 59th Electronic Components and Technology Conference*. San Diego, CA: IEEE, may 2009, pp. 831–836.

[15] Xingsheng Liu, Jingwei Wang, and Peiyong Wei, "Study of the mechanisms of spectral broadening in high power semiconductor laser arrays," in *2008 58th Electronic Components and Technology Conference*. Lake Buena Vista, FL: IEEE, may 2008, pp. 1005–1010.

[16] W. A. Clarkson, "Thermal effects and their mitigation in end-pumped solid-state lasers," *Journal of Physics D: Applied Physics*, vol. 34, no. 16, pp. 2381–2395, aug 2001.

[17] H. Bruesselbach, D. Sumida, R. Reeder, and R. Byren, "Low-heat high-power scaling using InGaAs-diode-pumped Yb:YAG lasers," *IEEE Journal of Selected Topics in Quantum Electronics*, vol. 3, no. 1, pp. 105–116, 1997.

[18] J. Lee and I. Mudawar, "Two-phase flow in high-heat-flux micro-channel heat sink for refrigeration cooling applications: Part IIheat transfer characteristics," *International Journal of Heat and Mass Transfer*, vol. 48, no. 5, pp. 941–955, feb 2005.

[19] J. D. Engerer and T. S. Fisher, "Flash boiling from carbon foams for high-heat-flux transient cooling," *Applied Physics Letters*, vol. 109, no. 2, p. 024102, jul 2016.

[20] E. Sher, T. Bar-Kohany, and A. Rashkovan, "Flash-boiling atomization," *Progress in Energy and Combustion Science*, vol. 34, no. 4, pp. 417–439, aug 2008.

[21] E. R. Dário, J. C. Passos, M. L. Sánchez Simón, and L. Tadrist, "Pressure drop during flow boiling inside parallel microchannels," *International Journal of Refrigeration*, vol. 72, pp. 111–123, dec 2016.

[22] N. Lior and A. Girbal-Puig, "The Integrated Heat Storage Flash Boiler (HSFB): Review, Principles, Design and Testing," in *Volume 6: Energy, Parts A and B*. ASME, nov 2012, p. 1457.

[23] M. A. Grolmes and H. K. Fauske, "Axial propagation of free surface boiling into superheated liquids in vertical tubes," *In: Heat transfer 1974; Proceedings of the Fifth International Conference, Tokyo, Japan, September 3-7, 1974. Volume 4. (A75-14226 03-34) Tokyo, Society of Heat Transfer of Japan, 1974, p. 30-34. AEC-sponsored research.*, vol. 4, pp. 30–34, 1974.

[24] P. Reinke and G. Yadigaroglu, "Explosive vaporization of superheated liquids by boiling fronts," *International Journal of Multiphase Flow*, vol. 27, no. 9, pp. 1487–1516, sep 2001.

[25] C. Price, A. Hamzehloo, P. Aleiferis, and D. Richardson, "Aspects of Numerical Modelling of Flash-Boiling Fuel Sprays," sep 2015.

[26] W.-l. Cheng, H. Chen, L. Hu, and W.-w. Zhang, "Effect of droplet flash evaporation on vacuum flash evaporation cooling: Modeling," *International Journal of Heat and Mass Transfer*, vol. 84, pp. 149–157, may 2015.

[27] J. D. Engerer, G. R. Jackson, R. Paul, and T. S. Fisher, "Flash Boiling and Desorption From a Macroporous Carbon-Boron-Nitrogen Foam," in *Volume 6B: Energy*. ASME, nov 2013, p. V06BT07A071.

[28] A. E. Siegman, *Lasers*. Sausalito: University Science Books, 1986.

[29] J. T. Verdeyen and J. Thomas, *Laser Electronics*, 3rd ed., N. J. Holonyak, Ed. New Jersey: Prentice Hall, 1995.

[30] O. Svelto, *Principles of lasers*. Springer, 2010.

[31] B. Zhao and A. Yariv, "Quantum well semiconductor lasers," in *Semiconductor Lasers I Fundamentals*, E. Kapon, Ed. San Diego: Academic Press, 1999, pp. 1–109.

[32] R. N. Hall, G. E. Fenner, J. D. Kingsley, T. J. Soltys, and R. O. Carlson, "Coherent light emission from GaAs junctions," *Physical Review Letters*, vol. 9, no. 9, pp. 366–368, 1962.

[33] D. J. Richardson, J. Nilsson, and W. A. Clarkson, "High power fiber lasers: current status and future perspectives [Invited]," *Journal of the Optical Society of America B*, vol. 27, no. 11, p. B63, nov 2010.

[34] C. Tang, "Quantum Electronics," in *Methods of Experimental Physics*. New York: Academic Press, 1979, vol. 15-PartA.

[35] B. R. Nag, *Physics of Quantum Well Devices*. Springer Netherlands, 2000.

[36] G. Erbert, A. Bärwolff, J. Sebastian, and J. Tomm, "High-Power Broad-Area Diode Lasers and Laser Bars," in *High-Power Diode Lasers Fundamentals, Technology, Applications*, R. Diehl, Ed. Springer Berlin Heidelberg, 2000, pp. 173–223.

[37] H. Sun, *A Practical Guide to Handling Laser Diode Beams*, ser. SpringerBriefs in Physics. Dordrecht: Springer Netherlands, 2015.

[38] H. Fritsche, F. Ferrario, R. Koch, B. Kruschke, U. Pahl, S. Pflueger, A. Grohe, W. Gries, F. Eibl, S. Kohl, and M. Dobler, "Direct diode lasers and their advantages for materials processing and other applications," F. Dorsch, Ed., vol. 9356. International Society for Optics and Photonics, mar 2015, p. 93560I.

[39] J. Horkovich, "Directed Energy Weapons: Promise and Reality," in *37th AIAA Plasmadynamics and Lasers Conference*. Reston, Virigina: American Institute of Aeronautics and Astronautics, jun 2006.

[40] J. Goings, P. Thiagarajan, D. Crawford, S. Smith, B. Caliva, and R. Walker, "Advancements of ultra-high peak power laser diode arrays," in *High-Power Diode Laser Technology XVI*, M. S. Zediker, Ed., vol. 10514. SPIE, feb 2018, p. 16.

[41] A. Gourevitch, B. Laikhtman, D. Westerfeld, D. Donetsky, G. Belenky, C. W. Trussell, Z. Shellenbarger, H. An, and R. U. Martinelli, "Transient thermal analysis of InGaAsP-InP high-power diode laser arrays with different fill factors," *Journal of Applied Physics*, vol. 97, no. 8, p. 084503, apr 2005.

[42] D. G. Mehuys, "High-Power Semiconductor Lasers," in *Semiconductor Lasers II Materials and Structures*, E. Kapon, Ed. San Diego: Academic Press, 1999, pp. 259–321.

[43] X. Liu, W. Zhao, L. Xiong, and H. Liu, *Packaging of High Power Semiconductor Lasers*. New York: Springer, 2015.

[44] A. Unger, W. Fassbender, H. Müntz, B. Köhler, and J. Biesenbach, "Beam shaping concepts for kW-class CW and QCW diode lasers," A. L. Glebov and P. O. Leisher, Eds., vol. 9730. International Society for Optics and Photonics, apr 2016, p. 97300H.

[45] H. Yu, Y. Liu, A. Braglia, G. Rossi, and G. Perrone, "Investigation of collimating and focusing lenses' impact on laser diode stack beam parameter product," *Applied Optics*, vol. 54, no. 34, pp. 10 240–10 248, dec 2015.

[46] ISO 11146-1, "Lasers and laser-related equipment Test methods for laser beam widths, divergence angles and beam propagation ratio," 2005.

[47] T. S. Ross and W. P. Latham, "Appropriate Measures and Consistent Standard for High Energy Laser Beam Quality (Postprint)," 2006.

[48] J. Huddle, L. Chow, S. Lei, A. Marcos, D. Rini, S. Lindauer, M. Bass, and P. Delfyett, "Thermal management of diode laser arrays," in *Sixteenth Annual IEEE Semiconductor Thermal Measurement and Management Symposium*, no. 407. IEEE, 2000, pp. 154–160.

[49] B. Laikhtman, A. Gourevitch, D. Westerfeld, D. Donetsky, and G. Belenky, "Thermal resistance and optimal fill factor of a high power diode laser bar," *Semiconductor Science and Technology*, vol. 20, no. 10, pp. 1087–1095, 2005.

[50] W. Engeler and M. Garfinkel, "Thermal characteristics of GaAs laser junctions under high power pulsed conditions," *Solid-State Electronics*, vol. 8, no. 7, pp. 585–604, jul 1965.

[51] T. Kobayashi and Y. Furukawa, "Temperature Distributions in the GaAs-AlGaAs Double-Heterostructure Laser below and above the Threshold Current," *Japanese Journal of Applied Physics*, vol. 14, no. 12, pp. 1981–1986, dec 1975.

[52] G. K. Veerabathran, S. Sprengel, S. Karl, A. Andrejew, H. Schmeiduch, and M.-C. Amann, "Transient thermal analysis of semiconductor diode lasers under pulsed operation," *AIP Advances*, vol. 7, no. 2, p. 025208, feb 2017.

[53] J. Michaud, G. Pedroza, L. Béchou, L. How, O. Gilard, D. Veyrié, F. Laruelle, and S. Grauby, "Investigations on electro-optical and thermal performances degradation of high power density GaAs-based laser diode in vacuum environment," *Microelectronics Reliability*, vol. 55, no. 9-10, pp. 1746–1749, aug 2015.

[54] C. Gooch, "Transient thermal effects in gallium arsenide injection lasers," *Physics Letters*, vol. 16, no. 1, pp. 5–6, may 1965.

[55] M. Ziegler, F. Weik, J. W. Tomm, T. Elsaesser, W. Nakwaski, R. P. Sarzała, D. Lorenzen, J. Meusel, and A. Kozłowska, "Transient thermal properties of high-power diode laser bars," *Applied Physics Letters*, vol. 89, no. 26, p. 263506, dec 2006.

[56] S. M. Sze, *Semiconductor Devices: Physics and Technology*. John Wiley & Sons, 2002.

[57] D. J. Konopa, "Thermal and Optical Characterization of High Power Laser Diodes," MS Thesis, Purdue University, 2016.

[58] H. I. Abdelkader, H. H. Hausien, and J. D. Martin, "Temperature rise and thermal risetime measurements of a semiconductor laser diode," *Review of Scientific Instruments*, vol. 63, no. 3, pp. 2004–2007, mar 1992.

[59] J. Pankove, "Temperature dependence of emission efficiency and lasing threshold in laser diodes," *IEEE Journal of Quantum Electronics*, vol. 4, no. 4, pp. 119–122, apr 1968.

[60] R. Puchert, A. Barwolff, M. Voss, U. Menzel, J. Tomm, and J. Luft, "Transient thermal behavior of high power diode laser arrays," *IEEE Transactions on Components and Packaging Technologies*, vol. 23, no. 1, pp. 95–100, mar 2000.

[61] A. R. Dhamdhere, A. P. Malshe, W. F. Schmidt, and W. D. Brown, "Investigation of reliability issues in high power laser diode bar packages," *Microelectronics Reliability*, vol. 43, no. 2, pp. 287–295, feb 2003.

[62] Z. Huang, L. Meng, H. Shen, Z. Han, and R. Zhu, "Analysis of influence of thermally induced aberrations on laser beam quality factor (M2) in a high-power laser system," *Optical Engineering*, vol. 57, no. 02, p. 1, feb 2018.

[63] D. Lorenzen, J. Bonhaus, W. Fahrner, E. Kaulfersch, E. Worner, P. Koidl, K. Unger, D. Muller, S. Rolke, H. Schmidt, and M. Grellmann, "Micro thermal management of high-power diode laser bars," *IEEE Transactions on Industrial Electronics*, vol. 48, no. 2, pp. 286–297, apr 2001.

[64] T. Mahefkey, K. Yerkes, B. Donovan, and M. L. Ramalingam, "Thermal Management Challenges For Future Military Aircraft Power Systems," nov 2004.

[65] R. N. Abed, "THE THERMAL MANAGEMENT SYSTEM OF LASER DIODE: A REVIEW," vol. 10, no. 12, 2015.

[66] M. B. Bowers and I. Mudawar, "Two-Phase Electronic Cooling Using Mini-Channel and Micro-Channel Heat Sinks: Part 2Flow Rate and Pressure Drop Constraints," *Journal of Electronic Packaging*, vol. 116, no. 4, p. 298, dec 1994.

[67] J. Lee and I. Mudawar, "Assessment of the effectiveness of nanofluids for single-phase and two-phase heat transfer in micro-channels," *International Journal of Heat and Mass Transfer*, vol. 50, no. 3-4, pp. 452–463, feb 2007.

[68] K. A. Estes and I. Mudawar, "Comparison of Two-Phase Electronic Cooling Using Free Jets and Sprays," *Journal of Electronic Packaging*, vol. 117, no. 4, p. 323, dec 1995.

[69] M. Visaria and I. Mudawar, "Application of Two-Phase Spray Cooling for Thermal Management of Electronic Devices," *IEEE Transactions on Components and Packaging Technologies*, vol. 32, no. 4, pp. 784–793, dec 2009.

[70] J. A. Ruff and A. E. Siegman, "Single-pulse laser beam quality measurements using a CCD camera system," *Applied Optics*, vol. 31, no. 24, p. 4907, aug 1992.

[71] D. C. Montgomery, *Design and Analysis of Experiments*. John Wiley & Sons, 2012.

[72] R. S. Pengelly, S. M. Wood, J. W. Milligan, S. T. Sheppard, and W. L. Pribble, "A Review of GaN on SiC High Electron-Mobility Power Transistors (HEMTs) and MMICs," *IEEE Transactions on Microwave Theory and Techniques*, vol. 60, no. 6, 2012.

[73] U. Mishra, P. Parikh, and Yi-Feng Wu, "AlGaN/GaN HEMTs-an overview of device operation and applications," *Proceedings of the IEEE*, vol. 90, no. 6, pp. 1022–1031, jun 2002.

[74] E. Heller and A. Crespo, "Electro-thermal modeling of multifinger AlGaN/GaN HEMT device operation including thermal substrate effects," *Microelectronics Reliability*, vol. 48, no. 1, pp. 45–50, jan 2008.

[75] W. J. Roesch, "Historical review of compound semiconductor reliability," *Microelectronics Reliability*, vol. 46, no. 8, pp. 1218–1227, aug 2006.

[76] E. Zanoni, "GaN HEMT reliability research a white paper ," 2017.

[77] J. A. Carter, J. Acord, D. Hoffmann, A. Trageser, and C. Pagel, "Thermal factors influencing the reliability of GaN HEMTs," in *2012 28th Annual IEEE Semiconductor Thermal Measurement and Management Symposium (SEMI-THERM)*. IEEE, mar 2012, pp. 182–188.

[78] M. Kuball, M. apajna, R. J. Simms, M. Faqir, and U. K. Mishra, "AlGaN/GaN HEMT device reliability and degradation evolution: Importance of diffusion processes," *Microelectronics Reliability*, vol. 51, no. 2, pp. 195–200, feb 2011.

[79] D. Cheney, E. Douglas, L. Liu, C.-F. Lo, B. Gila, F. Ren, and S. Pearton, "Degradation Mechanisms for GaN and GaAs High Speed Transistors," *Materials*, vol. 5, no. 12, pp. 2498–2520, nov 2012.

[80] G. D. Via, "GaN Reliability Where We Are and Where We Need to Go," *Proceedings of CS MANTECH Conference*, pp. 15–18, 2014.

[81] Y. Chou, D. Leung, I. Smorchkova, M. Wojtowicz, R. Grundbacher, L. Callejo, Q. Kan, R. Lai, P. Liu, D. Eng, and A. Oki, "Degradation of AlGaN/GaN HEMTs under elevated temperature lifetesting," *Microelectronics Reliability*, vol. 44, no. 7, pp. 1033–1038, jul 2004.

[82] E. Zanoni, G. Meneghesso, G. Verzellesi, F. Danesin, M. Meneghini, F. Rampazzo, A. Tazzoli, and F. Zanon, "A review of failure modes and mechanisms of GaN-based HEMTs," in *2007 IEEE International Electron Devices Meeting*. IEEE, 2007, pp. 381–384.

[83] J. Joh, F. Gao, T. Palacios, and J. A. del Alamo, "A model for the critical voltage for electrical degradation of GaN high electron mobility transistors," *Microelectronics Reliability*, vol. 50, no. 6, pp. 767–773, jun 2010.

[84] S. D. Burnham and B. M. Paine, "Towards an RF GaN Reliability Standard," in *JEDEC Reliability of Compound Semiconductors Workshop (ROCS)*, Indian Wells, CA, 2017.

[85] B. M. Paine, V. T. Ng, S. R. Polmanter, N. T. Kubota, and C. R. Ignacio, "Degradation rate for surface pitting in GaN HEMT," in *2015 IEEE International Reliability Physics Symposium*. IEEE, apr 2015, pp. CD.1.1–CD.1.7.

[86] B. M. Paine, S. R. Polmanter, V. T. Ng, N. T. Kubota, and C. R. Ignacio, "Lifetesting GaN HEMTs With Multiple Degradation Mechanisms," *IEEE Transactions on Device and Materials Reliability*, vol. 15, no. 4, pp. 486–494, dec 2015.

[87] B. M. Paine, "Scaling DC lifetests on GaN HEMT to RF conditions," *Microelectronics Reliability*, vol. 55, no. 12, pp. 2499–2504, dec 2015.

[88] O. Zienkiewicz and R. Taylor, *The Finite Element Method: Its Basis and Fundamentals*. Elsevier Science, 2005.

[89] A. Prejs, S. Wood, R. Pengelly, and W. Pribble, "Thermal analysis and its application to high power GaN HEMT amplifiers," in *2009 IEEE MTT-S International Microwave Symposium Digest*. IEEE, jun 2009, pp. 917–920.

[90] D. A. Gajewski, S. Sheppard, T. Mcnulty, J. B. Barner, J. Milligan, and J. Palmour, "RELIABILITY OF GaN / AlGaN HEMT MMIC TECHNOLOGY ON 100-mm 4H-SiC," *Cree*, pp. 141–145, 2011.

[91] D. A. Gajewski, S. Ganguly, S. Sheppard, S. Wood, J. B. Barner, J. Milligan, and J. Palmour, "Reliability comparison of 28 V50 V GaN-on-SiC S-band and X-band technologies," *Microelectronics Reliability*, vol. 84, pp. 1–6, 2018.

APPENDICES

A. DESIGN OF EXPERIMENTS DATA

Table A.1.
First DoX raw run parameters and data.

Block	Run	Factor 1 A:Anticipation (msec)	Factor 2 B:MeOHvol (mL)	Factor 3 C:Diodecurrent (A)	Response 1 Peak (nm)	Response 2 Spread (nm)
Day 1	1	-100	3	60	807.5	2.3
Day 1	2	-100	2	20	803.9	1.9
Day 1	3	175	3	100	811.2	2.7
Day 1	4	450	4	100	811.9	3.1
Day 1	5	1000	2	100	809.8	3.1
Day 1	6	1000	2	20	803.9	1.6
Day 1	7	-100	2	20	803.9	1.5
Day 1	8	450	4	60	808.5	2.1
Day 1	9	1000	4	20	806.5	1.6
Day 1	10	1000	4	20	806.0	1.5
Day 1	11	1000	2	100	811.0	2.9
Day 2	12	450	3	20	805.6	1.7
Day 2	13	1000	3	60	807.5	2.3
Day 2	14	1000	4	100	811.9	3.0
Day 2	15	-100	4	20	805.5	1.4
Day 2	16	-100	2	100	810.5	2.9
Day 2	17	-100	4	20	805.5	1.4
Day 2	18	-100	4	100	811.9	3.1
Day 2	19	450	2	60	806.5	2.3

Table A.2.

Second DoX raw run parameters and data.

Block	Run	Factor 1 A:Anticipation (msec)	Factor 2 B:MeOHvol (mL)	Factor 3 C:Diodecurrent (A)	Response 1 Peak (nm)	Response 2 Spread (nm)
Day 1	1	1000	1.5	60	807.1	2.6
Day 1	2	350	1.5	100	811.7	3.1
Day 1	3	350	2	60	807.3	2.6
Day 1	4	1000	2	20	804.3	1.8
Day 1	5	-300	2	100	812.0	3.2
Day 1	6	-228.5	1.5	38.4	805.1	2.2
Day 1	7	-300	1	20	803.1	1.9
Day 1	8	1000	1	100	811.7	3.1
Day 1	9	1000	1	100	811.7	3.1
Day 1	10	-300	1	20	803.3	1.9
Day 2	11	-300	2	20	804.1	2.1
Day 2	12	1000	1	20	803.1	2.2
Day 2	13	1000	2	100	812.7	3.2
Day 2	14	350	1	60	806.8	2.5
Day 2	15	350	1.75	20	803.9	1.8
Day 2	16	-300	1	100	812.0	3.2
Day 2	17	1000	1	20	803.4	2.0
Day 2	18	1000	2	100	812.0	3.3
Day 2	19	-300	1.5	82.4	809.8	2.8

Table A.3.
Final DoX raw run parameters and data.

Run	Factor 1 A:Anticipation (msec)	Factor 2 B:MeOHvol (mL)	Factor 3 C:Diodecurrent (A)	Response 1 Peak (nm)	Response 2 Spread (nm)	Response 3 Beam Quality (M^2)
1	0	2	100	809.5	2.8	112.6
2	0	1	20	803.3	1.5	69.7
3	505	1.5	20	803.4	1.5	71.0
4	265	2	20	804.3	1.8	68.1
5	550	1	60	805.6	2.3	90.9
6	0	2	100	809.0	2.7	99.4
7	1000	2	60	806.3	2.4	96.12
8	1000	1	100	808.3	2.7	95.1
9	800	2	20	804.9	1.7	68.2
10	775	1.5	60	806.1	2.2	97.8
11	455	2	60	806.3	2.2	99.2
12	0	1	20	803.6	1.4	69.2
13	1000	1	100	808.3	2.7	94.9
14	0	1.5	60	805.5	2.2	99.1
15	655	1.75	100	808.7	2.7	92.5
16	1000	1.25	20	803.8	1.4	71.7
17	0	1	100	808.3	2.7	92.4
18	0	1	100	808.3	2.6	87.6

B. MATLAB CODE

B.1   Beam Spectra Analysis

```matlab
1  close all
2  clear all
3  %Input user parameters
4  time = [0.5,1.0,2.0,5.0]; %desired time points, assuming ccs ...
       interval 500ms
5  num_runs = 1; %number of files you would like to import
6  make_plots = true; %decide if plots of all spectra should be made
7  save_figs = false; %choose whether to save figures
8  %Import data from lvm files. Name files starting with 'run_001.lvm'
9  %Get file names
10
11 num_cols = num_runs*4;
12 amplitude = zeros(3648,num_cols);
13 files = cell(1,num_runs);
14
15 for i = 1:num_runs
16 if i<10
17 files{i}= ['run_00' num2str(i) '.lvm'];
18 else
19 files{i}= ['run_0' num2str(i) '.lvm'];
20 end
21 file = uigetfile('.lvm','Select a file to plot') % for single file
22 run_data=load(file); % replace with files{i} for multiple files
23 for j = 1:length(time)
24 amplitude(1:3648,(4*(i-1))+j)=...
25 run_data(((3648*time(j)*2)+1):3648*((time(j)*2)+1),1);
```

```matlab
26 end
27 end
28
29 %Find wavelength of peak amplitude and FWHM
30 wavelengths = run_data(1:3648,2);
31 output = cell(3,4*num_runs+1);
32 output{1,1}='Run';
33 output{2,1}='Peak Wavelength (nm)';
34 output{3,1}='FWHM (nm)';
35 for i=1:num_runs
36 for j=1:4
37 output{1,(4*(i-1))+j+1}=...
38 ['Run ' num2str(i) ' ' num2str(time(j)) ' sec'];
39 output{2,(4*(i-1))+j+1}=...
40 maxwave(wavelengths,amplitude(1:3648,(4*(i-1))+j));
41 output{3,(4*(i-1))+j+1}=...
42 fwhm(wavelengths,amplitude(1:3648,(4*(i-1))+j));
43 end
44 end
45 display(output')
46 xlswrite('Flash_output',output)
47
48 %Generate plots of spectra for each run
49 if make_plots == true
50 for i = 1:num_runs
51 figure()
52 for j = 1:length(time)
53 plot(wavelengths,amplitude(1:3648,(4*(i-1))+j),'LineWidth',2);
54 hold on;
55 end
56 hold off
57 legend('0.5 sec','1.0 sec','2.0 sec','5.0 sec')
58 %title(['Run ' num2str(i) ' Spectrum']);
59 title('Run 8','fontsize',14);
60 xlabel('\lambda (nm)','fontsize',14);
```

```
61 ylabel('Relative Amplitude','fontsize',14);

62 axis([800 820 0 1.1])

63 set(gca,'fontsize',14)

64 if save_figs==true

65 savefig(['Run ' num2str(i) '.fig']);

66 end

67 end

68 end
```

B.2   Beam Profile Analysis

```
1  % Main file for batch analysis of beam image data. Averages raw ...
       image data

2  % together after user selects folders (for waist and far-field data)

3  % containing subfolders containing images of each run. Analysis ...
       only for

4  % y-profile. Outputs a .csv file with the following columns (runs ...
       sorted

5  % in order the folders are sorted):

6  %     M^2

7  %     Waist width (gaussian 1 term fit)

8  %     R^2 for 1 term waist fit

9  %     Far field width (gaussian 1 term fit)

10 %     R^2 for 1 term far field fit

11 %

12 % 9/01/2017   Evan Schlenker

13

14 %%%%%%%% User configurable inputs ...
       %%%%%%%%%%%%%%%%%%%%%%%%%%%%%%%%%%%%%%

15 zwaist = 225; % location of profiler for waist measurement

16 zfar = 260; % location of profiler for far field measurement

17 lambda=807; % diode operating wavelength
```

```matlab
18
19   xmin = -4386; xmax = 4379.55; % sensor dimension, microns
20   ymin = -3295.95; ymax = 3302.4; % sensor dimension, microns
21   numy = 1024; numx = 1360; % number of pixels
22   xlocs = linspace(xmin,xmax,numx)';
23   ylocs = linspace(ymin,ymax,numy)';
24
25   % Get directory information
26   waist_folder = uigetdir('','Select folder containing waist ...
         measurements');
27   waist_folders = dir(waist_folder);
28   waist_folders(1:2)=[];
29   far_folder = uigetdir('','Select folder containing far-field ...
         measurements');
30   far_folders = dir(far_folder);
31   far_folders(1:2)=[];
32
33   % Storage for output parameters
34   avg_waist = cell(length(waist_folders),1);
35   avg_far = cell(length(far_folders),1);
36   waist_calcs = cell(length(avg_waist),1);
37   waist_gauss1 = zeros(length(avg_waist),1);
38   waist_R2 = zeros(length(avg_waist),1);
39   far_calcs = cell(length(avg_far),1);
40   far_gauss1 = zeros(length(avg_far),1);
41   far_R2 = zeros(length(avg_far),1);
42   Msquared = zeros(length(avg_far),1);
43
44   % Perform averaging, profiling, width, and beam quality calculations
45   for ii = 1:length(Msquared)
46   avg_waist{ii}=AverageProfiles...
47   (fullfile(waist_folder,waist_folders(ii).name));
48   avg_far{ii}=AverageProfiles(fullfile(far_folder,far_folders(ii).name));
49   waist_calcs{ii}=VarianceCalcs_vector(avg_waist{ii},ylocs);
50   waist_gauss1(ii)=waist_calcs{ii}{1}(1);
```

```
51  waist_R2(ii)=waist_calcs{ii}{1}(2);
52  far_calcs{ii}=VarianceCalcs_vector(avg_far{ii},ylocs);
53  far_gauss1(ii)=far_calcs{ii}{1}(1);
54  far_R2(ii)=far_calcs{ii}{1}(2);
55  Msquared(ii)=BeamQualityCalc...
56  (zwaist,zfar,waist_gauss1(ii),far_gauss1(ii),lambda);
57  percent = ii*100/length(avg_waist);
58  disp(['Calculating results - ' num2str(percent,3) '% completed'])
59  end
60
61  % Output to .csv file
62  output=zeros(length(Msquared),5);
63  output(:,1)=Msquared(:);
64  output(:,2)=waist_gauss1(:); % 1 term gauss waist width
65  output(:,3)=waist_R2(:); % 1 term gauss waist R^2
66  output(:,4)=far_gauss1(:); % 1 term gauss far field width
67  output(:,5)=far_R2(:); % 1 term gauss far field R^2
68  csvwrite('BeamQualityOutput.csv',output)
```

```
1   function ave_y_prof = AverageProfiles(directory)
2   % Calculates the average transverse y profile over the 5 sec run
3   % Load images
4   files = dir(directory);
5   files(1:2) = [];
6   images = cell(length(files),1);
7   for i=1:length(files)
8   fullFileName = fullfile(directory, files(i).name);
9   images{i}=load(fullFileName);
10  end
11  % Calculate
12  all_data=cat(3,images{:});
13  ave_image = mean(all_data,3); %average images pixel to pixel
14  ave_y_prof = sum(ave_image')'; %create profile by summing along axis
```

```matlab
15  ave_y_prof = ave_y_prof - min(ave_y_prof); %background noise ...
       threshold
16  ave_y_prof = ave_y_prof/max(ave_y_prof); %normalize
```

```matlab
1   function output = VarianceCalcs_vector(profile,locations)
2   % Single output cell array, formatted as follows [sigma_gauss(var,R2)
3   % sigma_gauss2(var,R2) f1 sigma1 ]
4
5   output = cell(4,1);
6
7   % 1 term Gaussian fit
8   [f1, eval1] = fit(locations,profile,'gauss1');
9   coeff = coeffvalues(f1);
10  output{1} = [coeff(3),eval1.rsquare];
11  output{3} = f1;
12
13  %2 term Gaussian fit
14  [f2, eval2] = fit(locations,profile,'gauss2');
15  coeff2 = coeffvalues(f2);
16  output{2} = [coeff2(3) coeff2(6)];
17
18  %1 term variance and standard deviation
19  var1 = var(1:length(profile),profile); %compute variance (not ...
       from Gaussian fit)
20  sigma1 = sqrt(var1); %variance in pixels
21  sigma1 = sigma1*6.45; %variance in microns
22  output{4} = sigma1;
23  end
```

```matlab
1   function [Msquared] = BeamQualityCalc(z1,z2,sigma1,sigma2,lambda)
2   %Calculates beam quality using 2-point method.
```

```matlab
3  Msquared = ...
       (4*pi*sigma1*sigma2*10^-12)/(((z2-z1)*10^-3)*lambda*10^-9);
4  end
```

B.3 Arrhenius Model

```matlab
1  %% Inputs
2
3  single_ANSYS = false; % import channel temperatures from ANSYS ...
       export .txt
4  range_ANSYS = true; % import series of ANSYS runs from a directory
5  coldplate_temps = [5 15 25 35 45 55 65 75 85 95]; % in celsius, 4 ...
       W/mm
6
7  make_plots = false; % generate variable range-based figures
8  make_ANSYS_plots = true; % make plots for inputted ANSYS data
9
10 % For Range plots
11 low_temp = 140; % minimum temperature of range in celsius
12 high_temp = 340; % maximum temperature of range in celsius
13 low_volt = 28; % minimum of voltage stress range
14 high_volt = 60; % maximum of voltage stress range
15 volt_range = (low_volt:(high_volt-low_volt)/4:high_volt);
16 Ea_range = (1:(1.5-1)/4:1.5); % activation energy range in eV
17
18 % For evaluating ANSYS model lifetime
19 Ea1 = 0.8; % First failure mechanism activation energy (eV)
20 Ea2 = 1.1; % Second failure mechanism activation energy (eV)
21
22 % Arrhenius and failure equation parameters
23 A = 0.5; % pre-exponential factor, should be at most 1
24 %%% Add second prefactor term, can be a ratio of the first term
```

```matlab
25 Ea = 1.1; % Activation energy in eV
26 kb = 8.6173E-5; % Boltzmann constant in eV
27 V = 28; % Operating voltage
28 gamma = 1.5; % varies between 1 and 4.5
29
30 %% Load and process ANSYS channel temperatures
31 if single_ANSYS
32 file = uigetfile('.txt', 'Please select a text file for the ...
       channel temperatures');
33 data = dlmread(file, '', 1, 0);
34 nodes = data(:,1); temps = data(:,2);
35 temps = temps + 273.15; % convert celsius to kelvin
36 max_temp = max(temps); min_temp = min(temps); mean_temp = ...
       mean(temps);
37
38 % Single point calculations
39 C = 1/(A*V^gamma);
40 MTTF_mean = C.*exp(Ea./(kb.*mean_temp)); % MTTF in seconds
41 MTTF_mean = MTTF_mean/3600; % MTTF in hours
42 MTTF_max = C.*exp(Ea./(kb.*max_temp)); % MTTF in seconds
43 MTTF_max = MTTF_max/3600; % MTTF in hours
44 disp(max_temp); disp(MTTF_max);
45 disp(mean_temp); disp(MTTF_mean);
46 end
47
48 if range_ANSYS
49 ANSYS_dir = uigetdir('','Select varying temperature measurement ...
       directory');
50 ANSYSfiles = dir(ANSYS_dir);
51 ANSYSfiles(1:2) = []; % remove extra directory structs
52
53 ANSYS_data = cell(length(ANSYSfiles),4); % Each row has: ...
54 % Node Numbers, Temps, Mean Temp, Peak Temp, MTTF (for mean), ...
       MTTF (peak)
55 for i=1:length(ANSYSfiles)
```

```matlab
56  fullFileName = fullfile(ANSYS_dir, ANSYSfiles(i).name);
57  temp = dlmread(fullFileName, '', 1, 0);
58  ANSYS_data{i,1} = temp(:,1); % node numbers
59  ANSYS_data{i,2} = temp(:,2) + 273.15; % node temperatures in K
60  ANSYS_data{i,3} = mean(ANSYS_data{i,2}); % mean channel ...
        temperature (K)
61  ANSYS_data{i,4} = max(ANSYS_data{i,2}); % max channel temperature (K)
62  end
63
64  % Calculate Arrhenius rates
65  Aa = A*V^gamma;
66  ANSYS_rates = cell(size(ANSYS_data,1),6);
67  % k (mean) Ea1, k (mean) Ea2, k (mean) total, repeated for peak
68  for i=1:size(ANSYS_rates,1)
69  ANSYS_rates{i,1} = Aa*exp(-Ea1/(kb*ANSYS_data{i,3})); % use mean temp
70  ANSYS_rates{i,2} = Aa*exp(-Ea2/(kb*ANSYS_data{i,3})); % use mean temp
71  ANSYS_rates{i,3} = ANSYS_rates{i,1} + ANSYS_rates{i,2};
72  ANSYS_rates{i,4} = Aa*exp(-Ea1/(kb*ANSYS_data{i,4})); % use peak temp
73  ANSYS_rates{i,5} = Aa*exp(-Ea2/(kb*ANSYS_data{i,4})); % use peak temp
74  ANSYS_rates{i,6} = ANSYS_rates{i,4} + ANSYS_rates{i,5};
75  end
76
77  ANSYS_MTTF = zeros(size(ANSYS_data,1),6);
78  % MTTF mean Ea 1, MTTF mean Ea 2, MTTF mean combined ...
79  % MTTF peak Ea 1, MTTF peak Ea 2,  MTTF peak combined
80  ANSYS_MTTF = (1./cell2mat(ANSYS_rates))/3600;
81  end
82
83  % Plot MTTF for mean and average case (2 separate plots)
84  if make_ANSYS_plots
85
86  figure
87  semilogy(coldplate_temps, ANSYS_MTTF(:,1))
88  hold on
89  semilogy(coldplate_temps, ANSYS_MTTF(:,2))
```

```matlab
90  semilogy(coldplate_temps, ANSYS_MTTF(:,3))
91  hold off
92  ylabel('Mean Time to Failure (hours)')
93  xlabel('Coldplate Temperature (\circC)')
94  title('MTTF with Various Coldplate Temperatures - Mean Channel ...
        Temperature')
95  legend(['Ea =' num2str(Ea1)], ['Ea =' num2str(Ea2)], 'Combined ...
        Ea', 'Location','northwest')
96
97  figure
98  semilogy(coldplate_temps, ANSYS_MTTF(:,4))
99  hold on
100 semilogy(coldplate_temps, ANSYS_MTTF(:,5))
101 semilogy(coldplate_temps, ANSYS_MTTF(:,6))
102 hold off
103 ylabel('Mean Time to Failure (hours)')
104 xlabel('Coldplate Temperature (\circC)')
105 title('MTTF with Various Coldplate Temperatures - Peak Channel ...
        Temperature')
106 legend(['Ea =' num2str(Ea1)], ['Ea =' num2str(Ea2)], 'Combined ...
        Ea', 'Location','northwest')
107 end
```